FULL WAVE SYNTHETIC ACOUSTIC LOGS IN SATURATED POROUS MEDIA PART III: PORE SHAPE AND PORE GEOMETRY EFFECTS

by

D.P. Schmitt

Earth Resources Laboratory
Department of Earth, Atmospheric, and Planetary Sciences
Massachusetts Institute of Technology
Cambridge, MA 02139

Abstract

Homogenization theory states that the viscous and mass coupling coefficients of a fully saturated porous medium depend upon the pore shape and the pore geometry. Using an approximate formula, the three body wave velocities and attenuations are analyzed for different configurations. The results show a strong influence of the mass coupling coefficient on these properties. The greater it is, the less biphase the porous medium is. Hence, in the high frequency range, the body wave velocities and attenuations decrease. Using the discrete wavenumber method, synthetic microseismograms are computed in an axisymmetric water-filled borehole. In the presence of a given porous formation with a permeable interface, whatever the mass coupling coefficient, Stoneley wave attenuation and dispersion characteristics are only slightly affected. The reliability of the indirect permeability determination is then ensured. On the other hand, the pseudo-Rayleigh modes are less attenuated with increasing mass coupling coefficient. In the absence of any borehole fluid attenuation, they may become dominant with a high source center frequency. This emphasizes the requirement for low band pass frequency records to be able to easily determine the rheological parameters of a formation.
Complex geometries are shown which would allow one to take into account an anisotropic permeability distribution.

INTRODUCTION

The mass coupling coefficient ρ_{22} of a saturated porous formation medium is usually assumed to be frequency independent. It is related to the saturant fluid density ρ_f through the porosity $\tilde{\phi}$ and a tortuosity factor, θ, (Plona and Johnson, 1980):

$$\rho_{22} = \theta\tilde{\phi}\rho_f \qquad \text{with} \quad \theta \geq 1$$

High frequency measurements using either the acoustic index of refraction of superfluid ^{4}He or electrical conductivity (Johnson et al.,1982) well agree with theory. They

show that this coefficient is always greater than 1, which is the high frequency limit for a unidirectional cylindrical duct.

Bonnet (1985) carried out measurements of both viscous and mass coupling coefficients at low frequecies, up to the characteristic frequency f_c, of fused glass balls. Again, the measured value of the mass coupling coefficient does not correspond to that of the cylindrical duct. Furthermore, the value obtained for the viscous coupling coefficient itself also does not correspond to the one computed for the cylindrical duct.

Bedford et al. (1984), also show that for a given pore geometry the coupling coefficients depend on the pore orientation with respect to the fluid motion.

Homogenization theory (Auriault, 1980; 1981; Avallet, 1981; Borne, 1983; Auriault et al., 1985) states that the viscous and mass coupling coefficients are related to one another and depend on the pore shape and pore geometry. When these latter parameters are given, they may be computed or analytically evaluated by integration of the Navier-Stokes equations. Their interdependence occurs through a complex permeability function. These results have been confirmed by experimental measurements made in the whole frequency range for a porous medium whose pores are loop-holes (Borne, 1983; Auriault et al., 1985). It has to be mentioned that the relation so obtained for the mass coupling coefficient is analogous to the one of Plona and Johnson (1980) but with a tortuosity factor which is frequency dependent.

There are several reasons to investigate the effects of both coupling coefficients. They may explain the discrepancy between the experimental slow P_2 wave velocity and attenuation measurements and the computed values (Dutta, 1980; Berryman, 1980). Johnson et al. (1982) focused their attention on the velocity variation only. They may also allow one to find a quantitative relationship between the formation factor obtained from the resistivity measurements and the mass coupling coefficient (see Brown, 1980). Last, but not least, they may play a part on the Stoneley wave behavior when logging in saturated porous formations with a permeable interface, and thus on the reliabiliy of the permeability determination.

In this paper, some results of homogenization theory are first briefly reviewed. The body wave velocities and attenuations in a saturated porous formation are then analyzed for several pore shapes and pore geometries. An approximate formula is used. It allows a simple calculation for any configuration. Using the discrete wavenumber method, the behavior of synthetic full waveforms obtained in an axisymmetric waterfilled borehole is also investigated. The last part is devoted to the analysis of more complex geometries with which an anisotropic permeability distribution may be taken into account.

THEORY

Homogenization theory: some results

The homogenization process uses two scales: the microsocopic and the macroscopic. Their characteristic length, respectively l and L, are defined so that $\varepsilon = l/L$ is much less than one. The pore structure is assumed to be periodic. The geometry and the local parameters are then also periodic.

For a porous medium whose porosity is $\tilde{\phi}$, the classical definitions at the microscopic scale are:

$|\Omega|$ = total volume of the porous medium.

Ω_f = fluid field ($|\Omega_f| = \tilde{\phi}|\Omega|$)

Ω_s = solid field,

$\underline{v}$ = fluid microscopic velocity,

$\overline{\underline{v}}$ = complex conjugate of $\underline{v}$

so that the fluid macroscopic velocity is given by:

$$\underline{V} = \frac{1}{|\Omega|} \int_{\Omega_f} v \, d\Omega \tag{1}$$

As pointed out by Auriault et al. (1985), $\underline{V}$, which is a volume mean value, is also a flux, i.e. a Darcy velocity.

When the porous medium is rigid, one obtains (Auriault, 1980,1981):

$$\underline{V} = K(\omega) \, \nabla p \tag{2}$$

where p is the pore pressure.
When the porous medium is deformable, this last equation becomes:

$$\underline{V} - \tilde{\phi} \dot{u}_s = K(\omega) \, \{ \nabla p - \rho_f \ddot{u}_s \} \tag{3}$$

where

u_s is the displacement in the solid,

ρ_f is the saturant fluid density,

the dot notation indicates temporal derivative(s)

The motion equations then obtained , as well as the stress strain relations, are identical to those of Biot (1956b) (see Part I for discussion).

$K(\omega)$ is identical in both cases. It is a complex permeability function which, in the most general case, is a symmetric complex tensor of order two, positive and definite, which thus can be inverted. The "spectral signature" of the porous medium is defined by:

$$H(\omega) = H_1(\omega) + iH_2(\omega) = 1./K(\omega) \tag{4}$$

$H_1(\omega)$ and $H_2(\omega)$ can be physically interpreted in terms of dissipated viscous power and kinetic energy. For instance, equation (1) then becomes:

$$\nabla p = H_1(\omega)\underline{v} + \omega^{-1}H_2(\omega)\dot{v}$$

It corresponds to the balance of momentum.

The classical coupling coefficients are then given by:

$$\begin{cases} b(\omega) &= \tilde{\phi}^2 H_1(\omega) \\ \rho_{22}(\omega) &= \dfrac{\tilde{\phi}^2}{\omega} H_2(\omega) \\ \rho_{12}(\omega) &= \tilde{\phi}\rho_f - \rho_{22}(\omega) \\ \rho_{11}(\omega) &= (1-\tilde{\phi})\rho_s - \rho_{12}(\omega) \end{cases} \tag{5}$$

where ρ_s is the solid density.

The viscous $b(\omega)$ and mass $\rho_{22}(\omega)$ coupling coefficients are then frequency dependent and depend upon the pore shape and the pore geometry. In addition, contrary to what is usually stated, they are related to one another.

For an isotropic medium both at the microscopic and macroscopic scales, one obtains (Borne, 1983):

$$\begin{cases} H_1(\omega) &= \dfrac{\eta}{|\Omega|}\displaystyle\int_{\Omega_f} \frac{\partial v_i}{\partial y_j}\frac{\partial \overline{v}_i}{\partial y_j}\, d\Omega \\ H_2(\omega) &= \dfrac{\omega\rho_f}{|\Omega|}\displaystyle\int_{\Omega_f} \underline{v}\,\overline{\underline{v}}\, d\Omega \end{cases} \tag{6}$$

where

y is the microscopic spatial variable,

η is the saturant fluid dynamic viscosity.

Two geometries have been usually considered to define the viscous coupling coefficient independently from the mass coupling coefficient. They are the cylindrical duct and the plane slit. For such configurations, one can directly use the Navier-Stokes equations to obtain $K(\omega)$ at the macroscopic scale. As pointed out by Auriault et al. (1985), this comes from the fact that the direct boundary problem at the macroscopic level is identical to the local boundary problem over the period introduced by the homogenization process. Applying a pressure gradient along the flow direction, one then obtains (Biot, 1956b, and Part I):

- for the cylindrical duct of radius a:

$$K(\omega) = -\frac{\tilde{\phi}}{i\omega\rho_f} J_2\left\{ia\left(\frac{i\omega}{\nu}\right)^{\frac{1}{2}}\right\} / J_0\left\{ia\left(\frac{i\omega}{\nu}\right)^{\frac{1}{2}}\right\} \tag{7}$$

- for the plane slit of thickness $2a$:

$$K(\omega) = \frac{\tilde{\phi}}{i\omega\rho_f}\left\{1 - \frac{1}{a}\left(\frac{\nu}{i\omega}\right)^{\frac{1}{2}} \tanh\left[a\left(\frac{i\omega}{\nu}\right)^{\frac{1}{2}}\right]\right\} \tag{8}$$

where $\nu = \eta/\rho_f$ is the kinematic viscosity of the fluid.

For more complicated geometries, the homogenization process is necessary. The exact solution then needs computation using the finite element method (Borne, 1983). The principal results are:

- an increase of both the low and the high frequency limits of the mass coupling coefficient. For instance, one can easily demonstrate that for any parallel pores of constant section, the high frequency limit (then analogous to the tortuosity θ) is equal to 1 (Appendix, after Boutin, personal communication). This is the case for the cylindrical duct and the plane slit.

- Considering that Darcy's law has to be satisfied when ω approaches zero, whatever the pore shape and the pore geometry, one obtains the value of the characteristic pore dimension (a) as a function of the material permeability $(\tilde{k})$ as:

$$\lim_{\omega\to 0} b(\omega) = \eta\tilde{\phi}^2/\tilde{k} \tag{9}$$

  so that the radius of the cylindrical ducts, for instance, is given by:

$$a^2 = 8\tilde{k}/\tilde{\phi} \tag{10}$$

- In the high frequency range, $b(\omega)$ is proportional to the square root of the frequency. The curves differ only through a frequency shift of the point from which the coupling coefficients depart from their static values.

Approximate formula

Because of these results, Bonnet (1985) proposed an approximate formula, based on the cylindrical duct geometry. It only needs physical parameters which can be experimentally measured. Denoting the nondimensional mass coupling coefficient by:

$$\rho_{22}^*(\omega) = \rho_{22}(\omega)/(\tilde{\phi}\rho_f)$$

they are

$$\lim_{\omega \to 0} \rho_{22}^*(\omega) = \tilde{d} \tag{11}$$

$$\lim_{\omega \to \infty} \rho_{22}^*(\omega) = \tilde{e} \tag{12}$$

The frequency shift is taken into account through the introduction of a so called sinuosity factor $\tilde{\tau}$. It is introduced in the formula which gives the radius of the cylindrical duct. The equation (10) is written:

$$a^2 = 8\tilde{k}\tilde{\tau}/\tilde{\phi} \tag{13}$$

Doing so, the zero frequency limit of the viscous coupling coefficient (equation (8)) then becomes:

$$\lim_{\omega \to 0} b(\omega) = \frac{\eta \tilde{\phi}^2}{\tilde{k}\tilde{\tau}} \tag{14}$$

For any arbitrary pore shape the coupling coefficients in the whole frequency range are then given by:

$$\rho_{22}^*(\omega) = 3(\tilde{d} - \tilde{e})\, g^*(\omega) + \tilde{e} \tag{15}$$

$$b(\omega) = \tilde{\tau}\tilde{\phi}^2 H_1(\omega) \tag{16}$$

where

$H(\omega) = H_1(\omega) + iH_2(\omega) = 1./K(\omega)$ is computed for cylindrical pores with a sinuosity $\tilde{\tau}$ using equations (7) and (12). The formula for $b(\omega)$ comes from equation (9) and because Darcy's law has to be satisified, whatever the sinuosity is. If the sinuosity is not introduced that way, it will have the same consequences as the permeability.

$$g^*(\omega) = \frac{\tilde{\phi}^2 H_2(\omega)}{\omega \tilde{\phi} \rho_f} - 1$$

This formulation will be used. It has the advantage of allowing a simple theoretical calculation using experimental measurements. The uncertainty of these last is greater than the theoretical error which may be introduced. Borne (1983) has studied the effects on body wave velocities and attenuations with the exact formulation but only for one very high frequency.

NUMERICAL EXAMPLES

The coupling coefficients will be produced in a nondimensional form, i.e:

$$b^*(\omega) = b(\omega)/(\eta\tilde{\phi}^2/\tilde{k})$$
$$\rho_{22}^*(\omega) = \rho_{22}(\omega)/(\tilde{\phi}\rho_f)$$

The body wave attenuations will be produced in dB/λ which is proportional to the inverse of the quality factor. The attenuation coefficient will be measured in dB/m.

Sinuosity effects

Sinuosity effects are analyzed using a water saturated Berea sandstone (see Table 1). The permeability and the porosity are equal to 19% and 1 darcy respectively. The successive sinuosity values considered are 1., 1.5, 3.0, and 5.0. They will be referred to as case 1, 2, 3 and 4. This study allows one, in a way, to infer the influence of only the viscous coupling coefficient.

An increase in the sinuosity results only in a shift toward lower frequencies of the coupling coefficient curves (Figure 1a). This is due to the argument of the complex permeability function, i.e.:

$$i\sqrt{\frac{i\omega a^2}{\nu}} = i\sqrt{\frac{i\omega}{\nu}\frac{8\tilde{k}\tilde{\tau}}{\tilde{\phi}}}$$

The low and high frequency limits of the three body wave phase and group velocities remain unchanged (Figure 1 b). However, the intermediate variations are complex. For instance, the first inflexion point of the group velocity curves appears to be less pronounced when the sinuosity increases.

Whatever the sinuosity is, the zero frequency limit of the viscous coupling coefficient follows Darcy's law. The low frequency body wave attenuations are then identical (Figure 1c). The viscous dissipation increases with the sinuosity beyond the frequency for which $b(\omega)$ begins to be proportional to $\sqrt{\omega}$. At the same time, the mass coupling coefficient is slightly smaller. The associated forces will then be of the same order of magnitude for a "critical" frequency which increases with the sinuosity.

This reasoning is confirmed by the variations of the dB/λ attenuation of all three body waves. Subsequently, high frequency attenuation is greater as well as the attenuation coefficient (Figure 1d). However, the low frequency shift of the coupling coefficient curves is emphasized by a decoupling of the P_1 and S wave attenuation from the part which is proportional to the frequency (i.e., the low frequency range). It occurs at lower frequencies when the sinuosity increases. The flow is no longer uniform at lower frequencies. Lastly, the greater the sinuosity, the straighter the attenuation coefficient curve of the slow P_2 wave.

The principal effect of an increased sinuosity is then to shift to higher frequencies the "critical" frequency of the porous medium. It leads to greater body wave attenuations in the high frequency range. This behavior is independent of the formation mechanical parameters.

Simple geometries

Porous media characteristics

Figure 2 displays pore models with a unidirectional flow (perpendicular to the borehole wall) (after Borne, 1983; Auriault et al., 1985). They are: loop-hole (1), variable section (fictitious) (2), cylindrical ducts (3) and plane slits (4). Corresponding to a decrease in the coupling coefficient, the sinuosity is lowered so as to be less than 1 for the plane slit. The model (2) is called "fictitious" because the "real" sinuosity is 1.1 (Borne, 1983). Setting it equal to 1 allows the analysis of only the mass coupling coefficient effects.

The formation considered is a water saturated Teapot sandstone (see Table 1) whose porosity and permeability are equal to 30% and 1.9 darcy respectively. The *characteristic* frequency f_c given by:

$$f_c = \frac{\tilde{\phi}\eta}{2\pi\tilde{k}\rho_f} \tag{17}$$

is thus equal to 25.246 kHz.

The associated coupling coefficients are displayed in Figure 3a (the numbers refer to the same models as in Figure 3).

The mass coupling coefficient is the parameter which has the most important effect on the velocities (Figure 3b). When $\rho_{22}(\omega)$ increases, *all three body wave velocities decrease in the high frequency range.* The low frequency values remain unchanged so that the dispersion also decreases. This comes from the fact that as ρ_{22} increases, *the porous medium is less biphase*: the relative motion between the two phases is less important. The analytical expressions of the high frequency limit phase and group velocities of the three body waves are:

- for the shear wave

$$\lim_{\omega\to\infty} \beta^2 = \frac{N}{(1-\tilde{\phi})\rho_s + \tilde{\phi}\rho_f - \frac{\tilde{\phi}}{\tilde{e}}\rho_f}$$

- for the compressional waves of the first (α_1) and second (α_2) kind:

$$\lim_{\omega\to\infty} \alpha_1(\alpha_2) = \frac{P\rho_{22} + \tilde{R}\rho_{11} - 2\rho_{12}Q \pm \Delta}{2(\rho_{11}\rho_{22} - \rho_{12}^2)}$$

where

P, $\tilde{R}$, Q are the elastic coefficients of the porous medium as defined in Part I (eq. (16)) with $P = A + 2N$.

ρ_{11}, ρ_{12}, ρ_{22} denote the high frequency limits of the mass coupling coefficients as defined in equation (5);

and $\Delta = \left\{ (P\rho_{22} + \tilde{R}\rho_{11} - 2\rho_{12}Q)^2 - 4(\rho_{11}\rho_{22} - \rho_{12}^2)(P\tilde{R} - Q^2) \right\}^{\frac{1}{2}}$

If the formula is relatively simple for the shear wave velocity, this is not the case for the P_1 and P_2 wave velocities. However, one can observe that for the P_1 wave the velocity ratio of the different examples varies proportionally to $\left\{(1-\tilde{\phi})\rho_s + \tilde{\phi}\rho_f(1-1/e)\right\}$ as for the shear wave. For the slow P_2 wave, the proportionality coefficient is equal to $e^{-\frac{1}{2}}$. It corresponds in a way to the limits obtained by Johnson and Plona (1982) when the bulk modulus of the saturant fluid (K_f) is much less than that of the material (K_b) and that the shear modulus (N) is less than the bulk material of the constitutive grains (K_s); i.e:

$$\lim_{\omega\to\infty} \alpha_1^2 = \frac{K_b + 4N/3}{(1-\tilde{\phi}\rho_s + (1-\frac{1}{\tilde{e}})\tilde{\phi}\rho_f}$$

and

$$\lim_{\omega\to\infty} \alpha_2^2 = \alpha_f/\sqrt{\tilde{e}}$$

where α_f is the saturant fluid velocity.

The differences between the values deduced from the above expressions and those computed here does not exceed 5% and 10%, respectively.

In the low frequency range, both the attenuations in dB/λ (Figure 3c) and in dB/m (Figure 3d) are identical to one another. This is because $b(\omega)$ and the velocities are also identical.

The examples, (2) and (3), for which the sinuosity is the same, clearly show that increasing the mass coupling coefficient leads to an enhancement of the frictional forces. These last are then of the same order of magnitude as the viscous forces for a frequency which decreases when the mass coupling coefficient increases. The dB/λ attenuation maxima of the P_1 and S waves are then shifted toward lower frequencies. The shift observed in Figure 4c exactly corresponds to the one evaluated using the *critical* frequency formula, i.e:

$$f_{ci} = \frac{\eta\tilde{\phi}}{2\pi\tilde{d}\rho_f} \tag{18}$$

One obtains 14 and 18.9 kHz, respectively, for the fictitious variable section model (2) and the cylindrical duct model (3). The high frequency attenuations of all three body waves are therefore weaker when $\tilde{d}$ increases. Again this is because the porous medium is less biphase.

The critical frequencies evaluated for the loop-hole (1) and the plane slit (4) models from the above equation are respectively equal to 6.8 and 21 kHz. The discrepancies which can be noted with the curves (Figure 4c) are due only to the sinuosity. However, they are much less pronounced than in the first study. They are related to a similar variation of both the coupling coefficients and associated forces. For such a situation, the computed critical frequency is still a good approximation for the frequency at which the attenuations are maxima. Because of the discontinuity in the slope of the attenuations around the critical frequency, the P_1 and S wave high frequency attenuations are smaller when ρ_{22} increases significantly (if not, the viscous forces still play a part). On the other hand, the high frequency attenuation coefficient decreases with ρ_{22} only for values close to the critical frequencies. Beyond this value, the distribution may still be influenced by the viscous dissipation.

These examples clearly show the importance of the knowledge of both the viscous and mass coupling coefficients in order to correctly predict the body wave velocities and attenuations experimentally measured.

Synthetic microseismograms

The effects of these geometries on the full waveform acoustic logs are studied by considering an axisymmetric water-filled borehole. No intrinsic attenuation is taken into account. The synthetic microseismograms are computed using the discrete wavenumber method as described in Part II. They are compared for a 5.25 meter long offset. The characteristics of the equivalent elastic formations are given in Table 3. 1, 2, 3 and 4 still denote the pore models as displayed in Figure 2.

Figure 4 shows the results obtained at the center of a borehole whose radius is 10 cm, in the presence of water saturated Teapot sandstone with a permeable interface. The source center frequency is equal to 7.5 kHz. With a decreasing mass coupling coefficient, the internal dynamics of each waveform continuously vary. The greater the high frequency shear wave attenuation, the less the pseudo-Rayleigh wave is developed. At the same time, the relative amplitude of the P wave and associated leaky modes as well as that of the Stoneley wave increase. The behavior of the interface wave, which may be surprising, is also related to the shift toward lower frequencies of the critical frequency. Although the relative motion between the two phases is less (the porous medium is less biphase), it affects the Stoneley wave at lower frequencies where its energy is more important. It then follows a greater dissipation of relative energy especially close to the frequency where the biphase behavior of the porous medium is reached ($\simeq f_c/8$). The "useful" energy is, however, nearly equivalent. The waveforms obtained with a 2.5 kHz source center frequency (Figure 5) confirm these observations. The maxima of amplitude vary little from one case to another. The phase velocity is only very slightly affected. At such a frequency, the variation does not exceed 1%.

The influence of the source center frequency on the internal dynamics of the microseismograms is also shown in Figure 6. The source center frequency varies from 1.5 to 7.5 kHz by step of 750 Hz from top to bottom. Case A refers to the loop-hole model while case B refers to the cylindrical duct model. The lower shear wave attenuation and the lower critical frequency in case A lead to a lower frequency occurrence of the shear and trapped mode energies.

When the pores are sealed at the borehole wall, the Stoneley wave is relatively unaffected whatever the source center frequency f_s is (Figure 7 where $f_s = 7.5$ kHz; Figure 8 where $f_s = 2.5$ kHz.). Again, the internal dynamics of the microseismograms essentially characterize the high frequency shear wave attenuation variations. The lower this is, the more developed the pseudo-Rayleigh wavetrain is. The P wave and associated leaky mode relative amplitudes are then nearly constant from one case to another despite the increasing P_1 wave attenuation.

The microseismograms displayed in Figures 9 and 10, for which f_s is respectively equal to 7.5 kHz and 2.5 kHz, have been obtained in the presence of water saturated Berea sandstone (see Table 1, $\tilde{\phi} = 19\%$, $\tilde{k} = 1$ darcy). The borehole wall is permeable and the borehole radius is equal to 7 cm. The computed critical frequency, from equation (18), is equal to 8.3 kHz for the loop-hole model (1), 20.42 kHz for the fictitious model (2), 23 kHz for the cylindrical duct (3) and 25.5 for the plane slit (4). Whatever the source center frequency is, the comments made for the Teapot sandstone still hold. They are also true in the presence of slow formations for which the P_1 wave attenuation plays an important part through the P-wave leaky modes. The results mentioned can then be generalized to any porous formation saturated with a fluid such as water when the interface is permeable.

The identification of the permeable character of a saturated porous formation can then still be made through the attenuation and dispersion characteristics of the Stoneley wave, whatever the coupling coefficients are. The examples shown in this study emphasize the reliability and the "ease" of such a process when realized with a low center source frequency.

The limitation made upon the saturant fluid properties comes from the fact that when it is not very viscous and very compressible, the critical frequency does not play an important role. The borehole fluid efficiently drives the saturant fluid away from the borehole wall. The attenuation of the shear wave which results then supersedes the effects related to only the coupling coefficients. This is also true for the Stoneley wave characteristic modificications (see Part II). The synthetic microseismograms obtained with the permeable gas saturated Fox Hill sandstone (Figure 11, $\tilde{\phi} = 7.4\%$ and $\tilde{k} = 1$ millidarcy) at the center of a borehole whose radius is equal to 10 cm emphasize this phenomenon. The interface is permeable. The pores are modeled as loop-holes (1) and cylindrical ducts (3). The source center frequency is equal to 7.5 kHz. The wavetrains cannot be distinguished from one another. The same results have been obtained with a lower source center frequency and with porous formations whose critical frequencies

(here equal to 507.4 kHz (1) and 1408 kHz (3)) are reduced because of a permeability increase.

Complex geometries

Anisotropy of the permeability is an important problem for a possibly productive oilfield. At the moment, no satisfactory method of describing this anisotropy has been found from the point of view of wave propagation. The following examples are only the beginning of an answer.

From the point of view of Stoneley wave propagation, the distribution of non interconnected cylindrical ducts along perpendicular directions as shown in Figure 12 is a form of anisotropy. In such a configuration, the "spectral signature" of the porous medium $H^{(n)}(\omega)$ can be determined. In the Appendix, a demonstration is made for the high frequency range where the saturant fluid behaves like a perfect fluid. The results obtained can be applied to the whole frequency range (Boutin, personal communication). The result is:

$$H^{(n)}(\omega) = nH^{(1)}(\omega) \tag{19}$$

where

n denotes the number of perpendicular directions taken into account,

$H^{(1)}(\omega) = 1/K(\omega)$ is relative to the case of unidirectional cylindrical ducts as defined by equations (4) and (7).

The relations (19) and (5) imply that the coupling coefficients are given by:

$$b^{(n)}(\omega) = nb^{(1)}(\omega) \tag{20}$$

$$\rho_{22}^{(n)}(\omega) = n\rho_{22}^{(1)}(\omega) \tag{21}$$

As Darcy's law has to be satisfied when the frequency vanishes, equation (10) has to be written as:

$$a^2 = 8\, n\, \tilde{k}/\tilde{\phi} \tag{22}$$

Despite the similarity between equations (13) and (22), the number of directions n is not equivalent to the sinuosity. It comes from equation (21) relative to the mass coupling coefficient. This result is emphasized by the behavior of the water saturated Teapot sandstone characteristics computed with $n = 1$, 2, and 3 (these are the numbers indicated in the Figures). The variations of the viscous coupling coefficient are identical (Figure 13a to be compared with Figure 3a). The effects of the mass coupling coefficients on the phase and group veocities of the three body waves are also the same (Figure 13b

to be compared with Figure 3b). However, the critical frequencies computed from equation (18), equal to 6.3, 9.5 and 18.9 kHz respectively for n=1, 2 and 3, do not exhibit any significant differences from the ones evaluated using the dB/λ attenuation curves (Figure 13c). Furthermore, the distribution of the attenuations in dB/λ and in dB/m of the slow P_2 wave (Figure 13d) is more regular in the whole frequency range.

The use of the equation (22) for the pore radius value implies that the total permeability is considered to participate in the flow. No difference is made between the total and the effective permeability. No "dead flow" zone is taken into account. This is the reason why the answer is not complete.

A more complex (and more realistic) configuration is obtained by considering interconnected pores. The only simple solution which can be easily defined is the high frequency limit of the mass coupling coefficient. The theoretical developments are presented in the Appendix. The limit is:

$$\lim_{\omega \to \infty} \rho_{22}(\omega) = \tilde{\phi} \rho_f \frac{|\Omega_f|}{|\Omega_{fe}} \tag{23}$$

where $|\Omega_{fe}|$ denotes the fluid volume affected by the flow.
Thus the more "dead zones" the fluid has, the greater the limit is.

Figures 14a, b display examples of orthotropic materials which can be analyzed in that manner. For the case in Figure 14a one obtains:

$$\frac{|\Omega_f|}{|\Omega_{fe}|} = \frac{(\frac{l}{L}+3)^2+3}{(\frac{l}{L}+2)^2+4}$$

so that,

$$\lim_{\omega \to \infty} \rho_{22}(\omega) = \frac{3}{2}\tilde{\phi}\rho_f \quad \text{when} \quad \frac{l}{L} \to 0$$

while for the case in Figure 14b,

$$\frac{|\Omega_f|}{|\Omega_{fe}|} = 1 + \frac{4}{2+\frac{l}{L}}$$

so that

$$\lim_{\omega \to \infty} \rho_{22}(\omega) = 3\tilde{\phi}\rho_f \quad \text{when} \quad \frac{l}{L} \to 0$$

With these kinds of geometries, the modeled porous material comes closer to the real cases.

CONCLUSIONS

Homogenization theory states that the frequency dependent viscous and mass coupling coefficients of a saturated porous medium depend on the pore shape and pore geometry. An approximate formula can be derived to make the calculations in the whole frequency range. It needs only physical parameters which can be experimentally measured. The results so obtained can be summarized as follows:

- ♠ The consequences of an increase in only the mass coupling coefficients are numerous.
  - ♣ the porous medium is less biphase in the sense that the relative motion between the two phases is less pronounced;
  - ♣ the *critical* frequency for which the viscous forces are equivalent to the inertial ones decreases;
  - ♣ the phase and group velocities of all three body waves decrease in the high frequency range, their dispersion is then less pronounced;
  - ♣ the high frequency attenuation of all three body waves decreases;
- ♠ Variations in the viscous coupling coefficient result in a frequency shift. For a given mass coupling coefficient, if the shift goes toward lower frequencies, the viscous forces increase. The attenuation (dB/λ) maxima of both P_1 and S waves is then shifted toward higher frequencies. The high frequency attenuation of all three body waves thus increases.
- ♠ Whatever the modified coupling coefficient is, the low frequency attenuations of all three body waves remain unchanged (Darcy's law).

These results emphasize the need of experimental measurements of both viscous and mass coupling coefficients of porous materials.

In the examples presented, when the mass coupling coefficient increases, the viscous coupling coefficient curve is shifted toward lower frequencies. The critical frequency is also shifted toward lower frequencies. The high frequency variations of the attenuations of all three body waves may be complex for similar mass coupling coefficient values.

Whatever the mass coupling coefficient is, Stoneley wave dispersion and attenuation are still representative of the permeability of a saturated porous formation when the borehole wall is permeable. However, this estimation will be all the more reliable if low frequency measurements can be done. This is because of the shear wave attenuation variations and correlated pseudo-Rayleigh mode behaviors.

Future theoretical developments should allow more realistic models where the anisotropy of the permeability would be taken into account.

ACKNOWLEDGEMENTS

I am indebted to Prof. J.L. Auriault, Dr. G. Bonnet and C. Boutin for many valuable and helpful discussions. I would like to thank Prof. M.N. Toksöz, Dr. C.H. Cheng and Dr. R.H. Wilkens for constructive and stimulating comments. This work was supported by the Société Nationale Elf Aquitaine (Production) and the Centre de Calcul Vectoriel pour la Recherche.

REFERENCES

Auriault, J.L., 1980, Dynamic behaviour of a porous medium saturated by a newtonian fluid. Int. J. Eng. Sci., 18, 775-785.

————,1980, Homogénéistaion: Application aux milieux poreux saturés, Cours de DEA Mécanique, Grenoble.

————, 1981, Homogenization. Application to porous saturated media. in *Two Medium Mechanics*, Summer School, Gdansk, 5-9 September.

Auriault, J.L., Borne, L., and Chambon, R., 1985, Dynamics of porous saturated media, checking of the generalized law of Darcy. J. Acoust. Soc. Am., 77, 1641-1650.

Avallet, C.,1981, Comportement dynamique de milieux poreux satures. These D.I. Grenoble Univ.

Bedford, A., Costley, R.D., and Stern, 1984, On the drag and virtual mass coefficients in Biot's equation, J. Acoust. Soc. Am., 76, 1804-1809.

Berryman, J.G., 1980, Confirmation of Biot's theory. Appl. Phys. Letters, 37 , 382-384.

Biot, M.A., 1956 a, Theory of propagation of elastic waves in a fluid saturated porous solid. I. Low frequency range. J. Acoust. Soc. Am., 28, 168-178.

———, 1956 b, Theory of propagation of elastic waves in a fluid saturated porous solid. II. Higher frequency range. J. Acoust. Soc. Am., 28, 179-191.

Bonnet, G., 1985, Contribution a l'etude des milieux poreux satures en regime dynamique. These d'Etat. Montpellier Univ.

Borne, L., 1983, Contribution a l'etude du comportement dynamique des milieux poreux satures deformables. Etude de la loi de filtration dynamique. These D.I. Grenoble Univ.

Brown, R.J.S., 1980, Connection between formation factor for electrical resistivity and fluid-solid coupling factor in Biot's equation for acoustic waves in fluid filled porous media. Geophysics, 45, 1269-1275.

Dutta, N.C., 1980, Theoretical analysis of observed second bulk compressional wave in a fluid saturated porous solid at ultrasonic frequencies. Appl. Phys. Lett., 37, 898-900.

Johnson, D.L., Plona, T.J., Scala, C., Pasierb, F., and Kojima, F., 1982 , Tortuosity and acoustic slow waves. Phys. Rev. Lett., 49, 1840-1844.

Johnson, D.L., and Plona, T.J., 1982, Acoustic slow waves and the consolidation transition. J. Acoust. Soc. Am. 72, 556-565.

Plona, T.J., and Johnson, D.L., 1980, Experimental study of the two bulk compressional modes in water saturated porous structures. Ultrasonic Symposium, 864-872.

Schmitt, D.P., 1985, Simulation numérique de diagraphies acoustiques. Propagation d'ondes dans des formations cylindriques axisymetriques radialement stratifiées incluant des milieux élastiques et/ou poreux saturés. Ph.D. thesis. Grenoble Univ.

————, 1986, Full wave synthetic acoustic logs in saturated porous media. Part I: Biot's theory. This issue.

————, 1986, Full wave synthetic acoustic logs in saturated porous media. Part II: Simpe configuration. This issue.

APPENDIX

High frequency study of the coupling coefficients

Using equation (6), the high frequency limit of $\rho_{22}(\omega)$ and $b(\omega)$ can be analytically studied.

In the very high frequency range, the calculations are much easier. The fluid behaves like a perfect fluid. The field of the microscopic velocities thus corresponds to a unit macroscopic velocity. It yields (from equation (1)):

$$V = 1 = \frac{1}{|\Omega|} \int_{\Omega_f} v \, d\Omega \tag{A.1}$$

Parallel ducts of any constant section

The Figure A.1 shows the porous medium geometry:

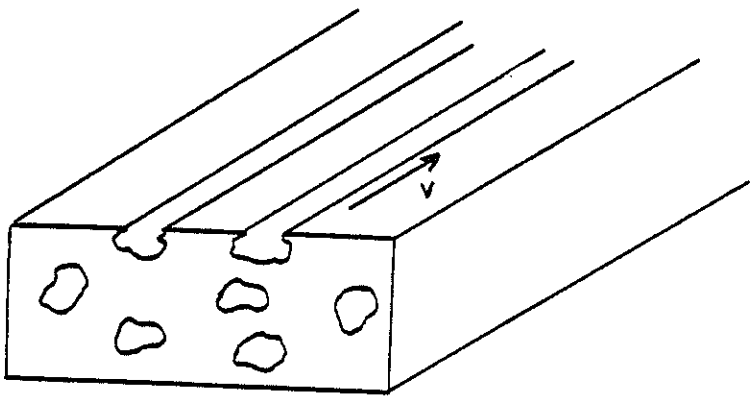

The unidirectional microscopic velocity field is constant in the pore section along the flow direction. Whatever the pore section is, equation (A.1) may then be written as:

$$V = 1 = \frac{v}{|\Omega|} \int_{\Omega_f} d\Omega_f = v \frac{|\Omega_f|}{|\Omega|} = v\tilde{\phi}$$

$$\Longleftrightarrow v = \frac{1}{\tilde{\phi}} \tag{A.2}$$

Putting this relation into equation (6), one obtains:

$$\lim_{\omega \to \infty} H_2(\omega) = \omega \rho_f v^2 \frac{|\Omega_f|}{|\Omega|} = \frac{\omega}{\tilde{\phi}} \rho_f$$

so that,

$$\lim_{\omega\to\infty} \rho_{22}(\omega) = \tilde{\phi}\rho_f = \rho_2 \tag{A.3}$$

Therefore, for a unidirectional flow, whatever the shape of the parallel pore sections, the high frequency limit of the mass coupling coefficient is equal to the density per unit volume of the porous medium of the saturant fluid. It corresponds to that obtained with cylindrical ducts (Appendix of Part I) and with plane slits (see text).

Constant section ducts, which are not connected, distributed along perpendicular directions

The most general case corresponds to (cylindrical) ducts distributed along three perpendicular directions. Figure 12 shows the porous medium structure. For generality, n will denote the geometric dimension (i.e., the number of directions taken into account).

Mass coupling coefficient

Because of isotropy, one only needs to determine the microscopic velocity field which corresponds to a macroscopic velocity field along a given direction. For the borehole geometry, this direction is perpendicular to the borehole wall. In order to be consistent with Figure 12, that direction will be denoted by Ox so that $\underline{V} = (1,0,0)^T$. Only the ducts in the Ox direction are affected by the flow. For the other directions, the microscopic velocity is equal to zero. Equation (A.1) may then be written as:

$$V = 1 = \frac{|\Omega_{fe}|}{|\Omega|} v_x \tag{A.4}$$

where $|\Omega_{fe}|$ denotes the fluid volume affected by the flow. Because of the material isotropy:

$$|\Omega_{fe}| = \frac{1}{n}|\Omega_f| \tag{A.5}$$

so that,

$$v_x = n/\tilde{\phi} \tag{A.6}$$

and

$$\lim_{\omega\to\infty} H_2(\omega) = \omega\rho_f v_x^2 \frac{|\Omega_{fe}|}{|\Omega|} = \omega\rho_f n/\tilde{\phi}$$

Hence:

$$\lim_{\omega\to\infty} \rho_{22}(\omega) = n\tilde{\phi}\rho_f = \rho_2 \tag{A.7}$$

For $n = 1$, the equation (A.3) is again verified.

Viscous coupling coefficient

The viscosity phenomena which occur at the pore wall where the flow takes place must be taken into account. Usually, a limiting plane layer whose thickness tends to zero with increasing frequency is considered. In addition, the curvature is neglected. Figure A.2 shows the situation for a flow direction along Ox:

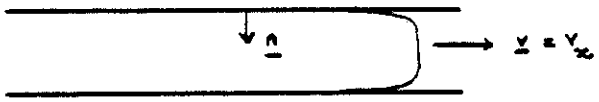

The determination of the corrective term is classical. One enforces as a limiting condition that:

- $\underline{v} = 0$ for $y = 0$. This is the adhesive condition.
- $\underline{v} = \underline{v}_{corrected}$ when y tends to infinity. This is the velocity continuity condition.

The Oz axis being taken so that the Oxyz reference is direct, one obtains:

$$v_c = v_x \left(1 - e^{-\sqrt{\frac{i\omega}{\nu}}y}\right)$$

$$\Longleftrightarrow \qquad v_c = v_x \left(1 - e^{-(1+i)\sqrt{\frac{\omega}{2\nu}}y}\right) \tag{A.8}$$

where $\nu = \eta/\rho_f$ is the kinematic viscosity of the fluid.
From this last relation, one deduces:

$$\overline{v}_c = v_x \left(1 - e^{-(1-i)\sqrt{\frac{\omega}{2\nu}}y}\right)$$

The equation (6) may then be written:

$$\lim_{\omega\to\infty} H_1(\omega) = \frac{\eta}{|\Omega|} \int_{|\Omega_f|} \frac{\partial v_c}{\partial y} \frac{\partial \overline{v}_c}{\partial y}\, d\Omega$$

$$\lim_{\omega\to\infty} H_1(\omega) = \frac{\eta}{|\Omega|} \int_{\Omega_f} v_x^2 \frac{\omega}{\nu} e^{-2\sqrt{\frac{\omega}{2\nu}}y}\, d\Omega \tag{A.9}$$

The volume integral can be separated:

$$\lim_{\omega\to\infty} H_1(\omega) = \frac{\eta}{|\Omega|} \int_{S_e} \int_0^\infty v_x^2 \frac{\omega}{\nu} e^{-2\sqrt{\frac{\omega}{2\nu}}y}\, dy\, dS \tag{A.10}$$

where S_e denotes the surface affected by the flow.

As for the study of the mass coupling coefficient, v_x is constant. Because:

$$\int_0^\infty e^{-\sqrt{\frac{\omega}{2\nu}}y}\, dy = \sqrt{\frac{\omega}{2\nu}}$$

one obtains:

$$\lim_{\omega\to\infty} H_1(\omega) = \frac{\eta}{|\Omega|} S_e v_x^2 \sqrt{\frac{\omega}{2\nu}}$$

Using the relations (5) and (A.1) yields:

$$\lim_{\omega\to\infty} b(\omega) = \tilde{\phi}\sqrt{\frac{\omega\eta\rho_f}{|\Omega|}}\,\frac{S_e}{|\Omega_{fe}|}\,\frac{|\Omega_f|}{|\Omega_{fe}|} \tag{A.11}$$

In the case of cylindrical ducts whose radius is a:

$$\frac{S_e}{|\Omega_{fe}|} = \frac{2\pi a l}{\pi a^2 l} = \frac{2}{a}$$

so that:

$$\lim_{\omega\to\infty} b(\omega) = \frac{2n}{a}\tilde{\phi}\sqrt{\frac{\omega\eta\rho_f}{2}} \tag{A.12}$$

For a monodimensional distribution, $n = 1$. The limit is then equal to that obtained with the cylindrical duct in the Appendix of Part I.

Any constant section interconnected pores

When the ducts are interconnected, the flow will remain rectilinear and uniform. If the limiting layer (whose thickness tends to zero) is assumed to behave rectilinearly and uniformly, the calculation can be performed. This is an approximation which is valid only at very high frequencies and when the characteristic pore dimension ratio l/L tends to zero. In Figure A.3, the dashed lines point out the real profile of the flow.

With this approximation, the constant microscopic velocity v is given by the relation (A.1) so that the equation (6) may be written:

$$\lim_{\omega\to\infty} H_2(\omega) = \frac{\omega\rho_f}{\tilde{\phi}}\,\frac{|\Omega_f|}{|\Omega_{fe}|} \tag{A.13}$$

and from the relation (5):

$$\lim_{\omega\to\infty} \rho_{22}(\omega) = \tilde{\phi}\rho_f\,\frac{|\Omega_f|}{|\Omega_{fe}|} \tag{A.14}$$

Two examples of orthotropic media are presented in the text.

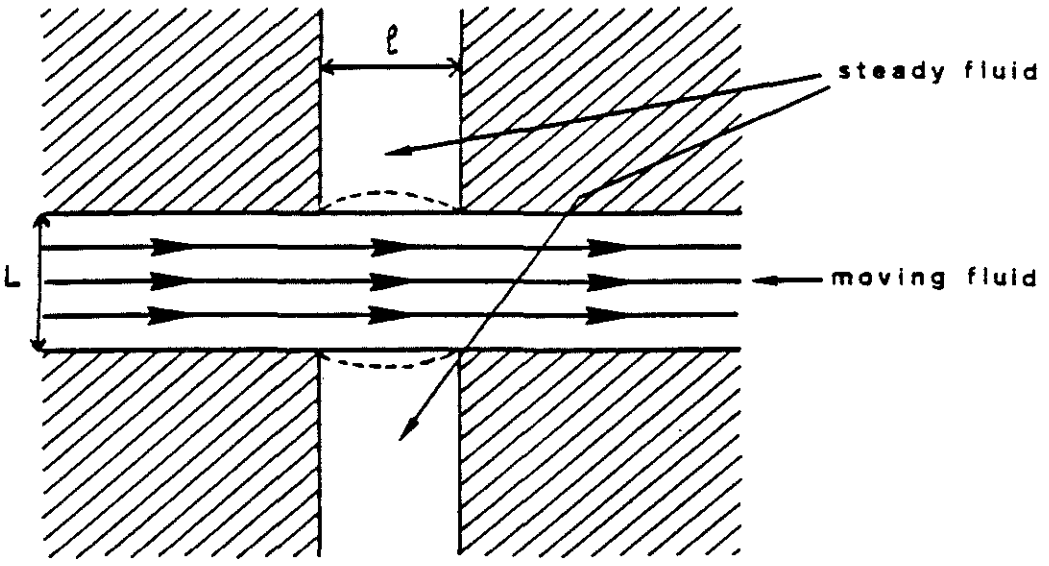

Figure A. 3

TABLE 1

Formations parameters

Name	K_s (Pa)	ρ_s (kg m^{-3})	α_m (ms^{-1})	β_m (ms^{-1})	$\tilde{\phi}$ (%)	$\tilde{k}$ (Darcy)
Berea Sandstone [1]	3.79 10^{10}	2650	3670	2170	19	1.
Fox Hill sandstone [1]	3.79 10^{10}	2650	4450	2515	7.4	0.0325
Teapot sandstone [1]	3.79 10^{10}	2650	3048	1865	29.7	1.9

[1] From Rosenbaum (1974)

TABLE 2

Saturant fluid parameters

Name	α_f (ms^{-1})	ρ_f (kg m^{-3})	η (cp)
Water	1500	1000	1.
Gas [1]	629.7	139.8	0.022

[1] From Rosenbaum (1974)

TABLE 3

Equivalent elastic formation parameters

Formation	Fluid	$\tilde{\phi}$ %	α (ms^{-1})	β (ms^{-1})	ρ ($kg\ m^{-3}$)	ν
Berea sandstone	Water	19	3735.8	2080.0	2336.5	0.275
Fox Hill sandstone	Gas	7.4	4443.0	2509.7	2464.2	0.266
Teapot sandstone	Water	29.7	3149.0	1732.0	2160.0	0.281

ν denotes Poisson's ratio

FIGURES

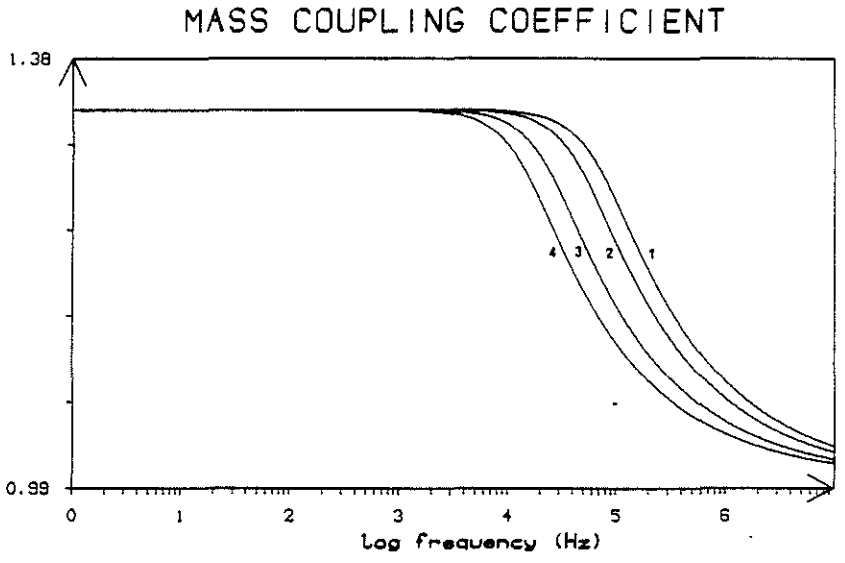

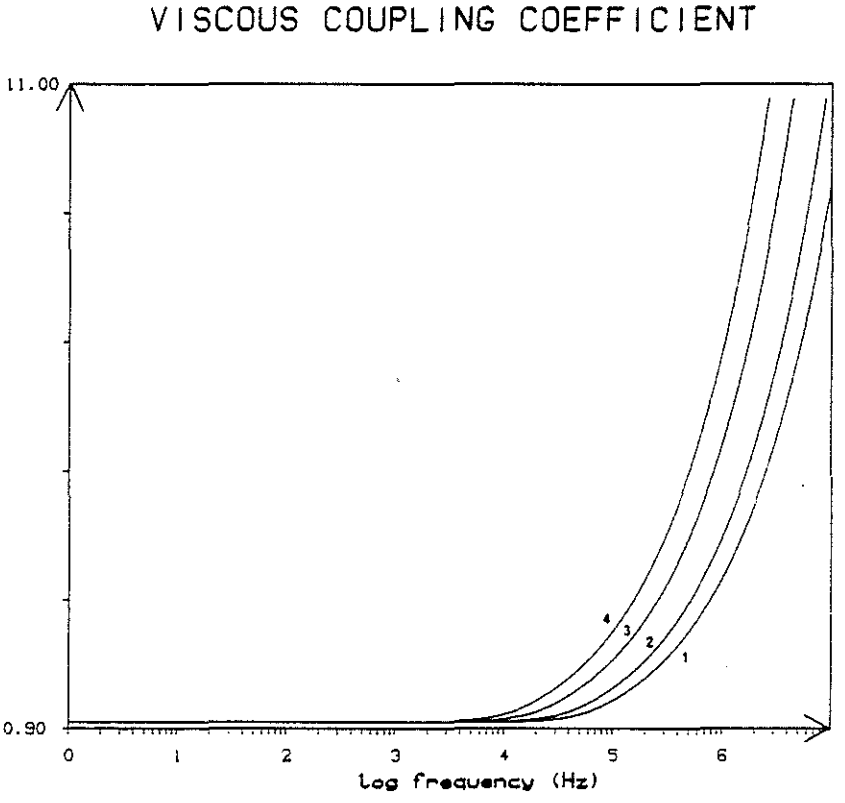

Figure 1a: Water saturated Berea sandstone. $\tilde{\phi} = 19\%$, $\tilde{k} = 1$ darcy. Sinuosity ($\tilde{\tau}$) effects. 1: $\tilde{\tau} = 1$, 2: $\tilde{\tau} = 1.5$, 3: $\tilde{\tau} = 3.$, 4: $\tilde{\tau} = 5.$.
Normalized coupling coefficients $(\rho_{22}(\omega)/(\tilde{\phi}\rho_f\ ; b(\omega)/(\eta\tilde{\phi}^2/\tilde{k}))$

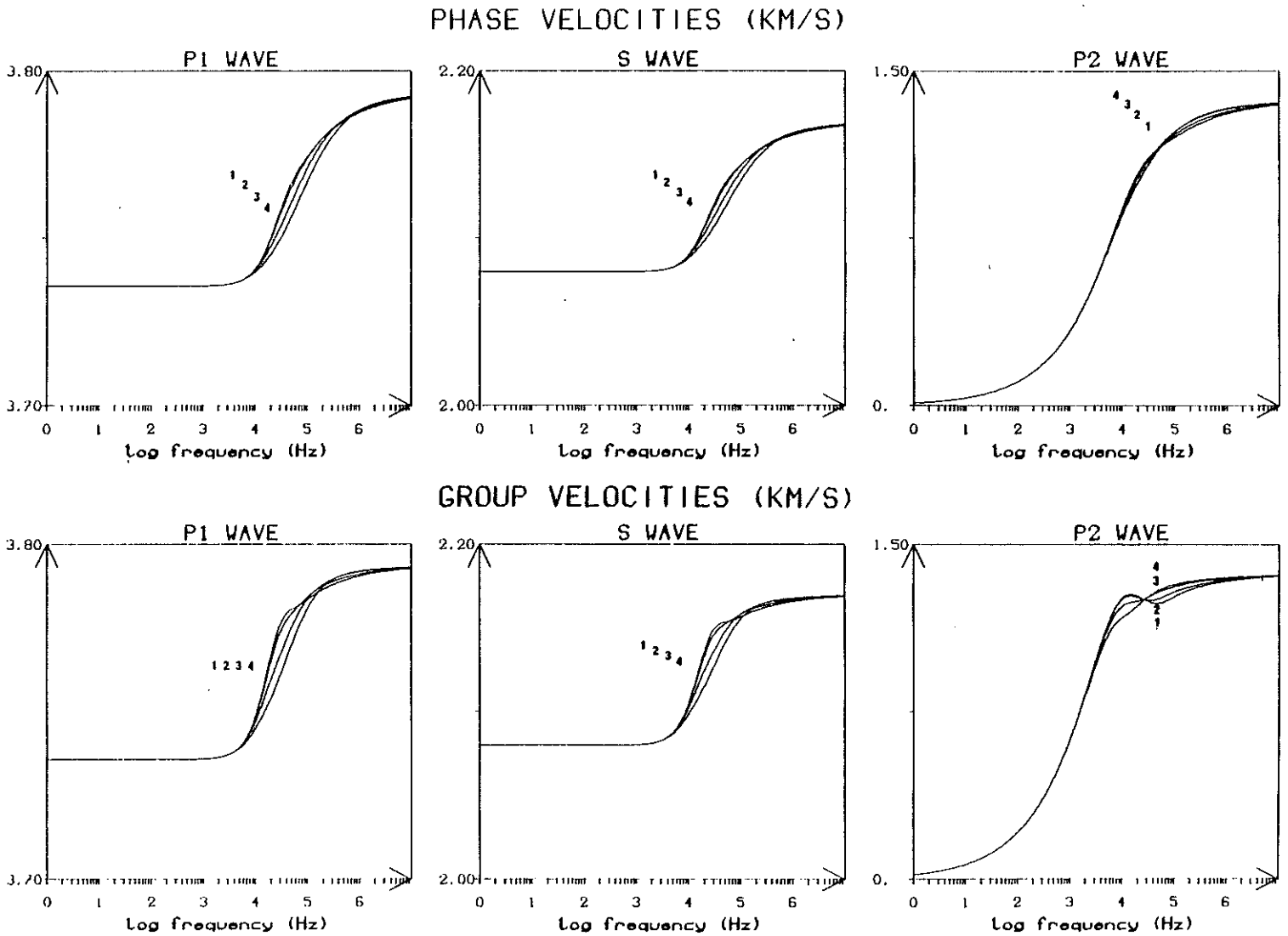

Figure 1b: Water saturated Berea sandstone. $\tilde{\phi} = 19\%$, $\tilde{k} = 1$ darcy. Sinuosity ($\tilde{\tau}$) effects. 1: $\tilde{\tau} = 1$, 2: $\tilde{\tau} = 1.5$, 3: $\tilde{\tau} = 3.$, 4: $\tilde{\tau} = 5.$.
Phase and group velocities of the body waves (P_1, S, P_2)

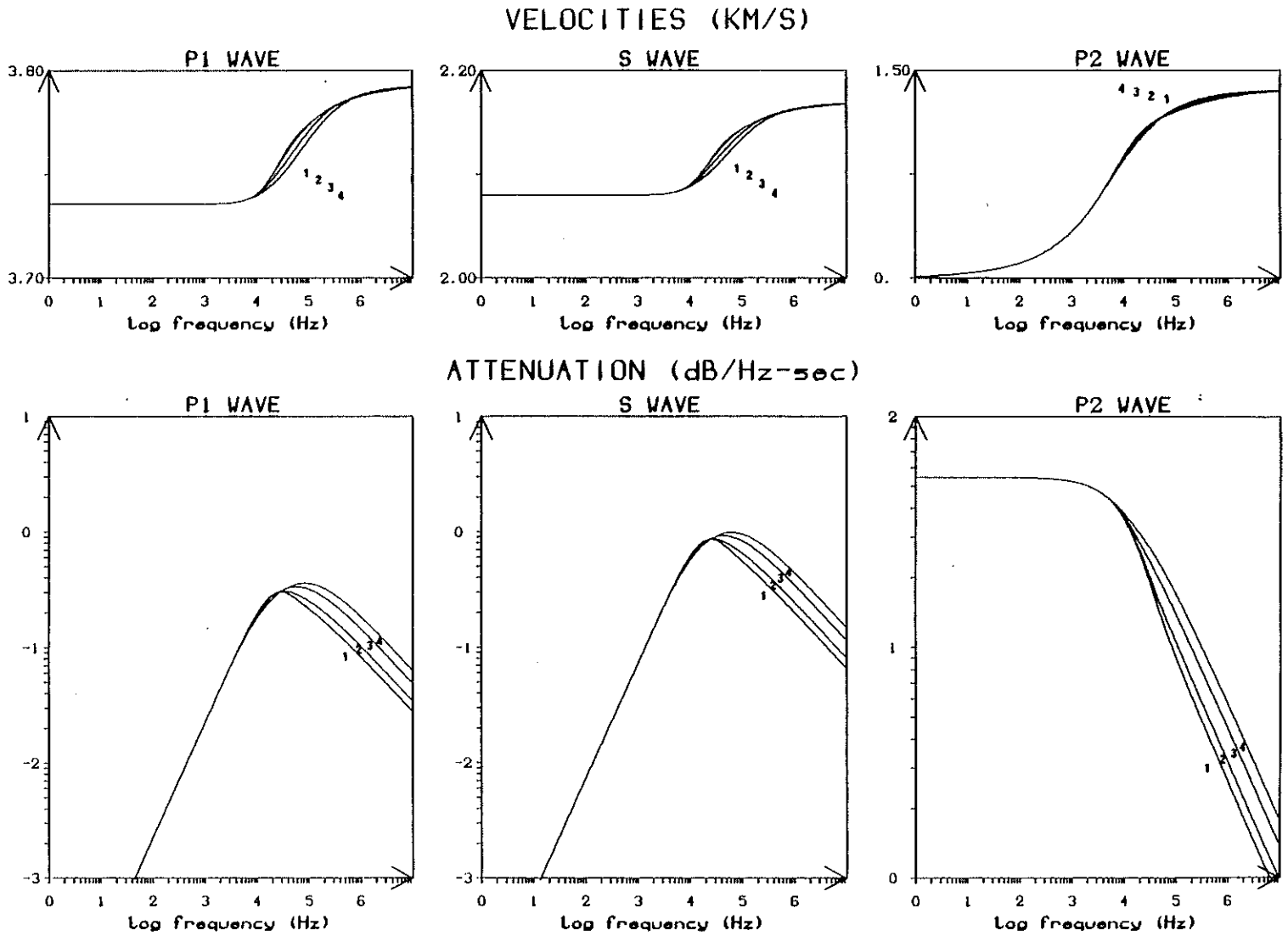

Figure 1c: Water saturated Berea sandstone. $\tilde{\phi} = 19\%$, $\tilde{k} = 1$ darcy. Sinuosity ($\tilde{\tau}$) effects. 1: $\tilde{\tau} = 1$, 2: $\tilde{\tau} = 1.5$, 3: $\tilde{\tau} = 3.$, 4: $\tilde{\tau} = 5.$.
Phase velocities and attenuations (dB/λ) of the body waves

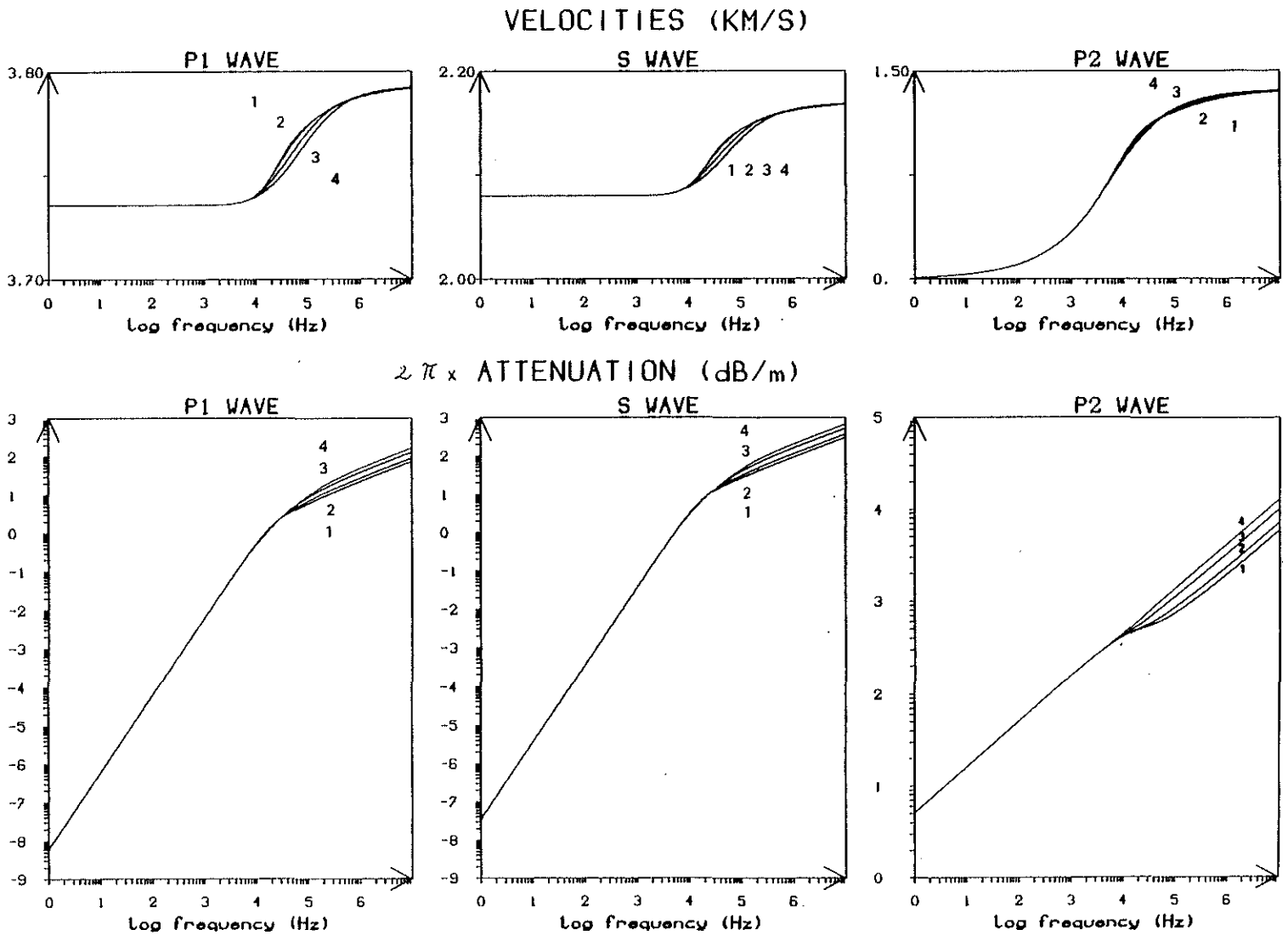

Figure 1d: Water saturated Berea sandstone. $\tilde{\phi} = 19\%$, $\tilde{k} = 1$ darcy. Sinuosity ($\tilde{\tau}$) effects. 1: $\tilde{\tau} = 1$, 2: $\tilde{\tau} = 1.5$, 3: $\tilde{\tau} = 3.$, 4: $\tilde{\tau} = 5.$.
Phase velocities and attenuations (dB/m) of the body waves

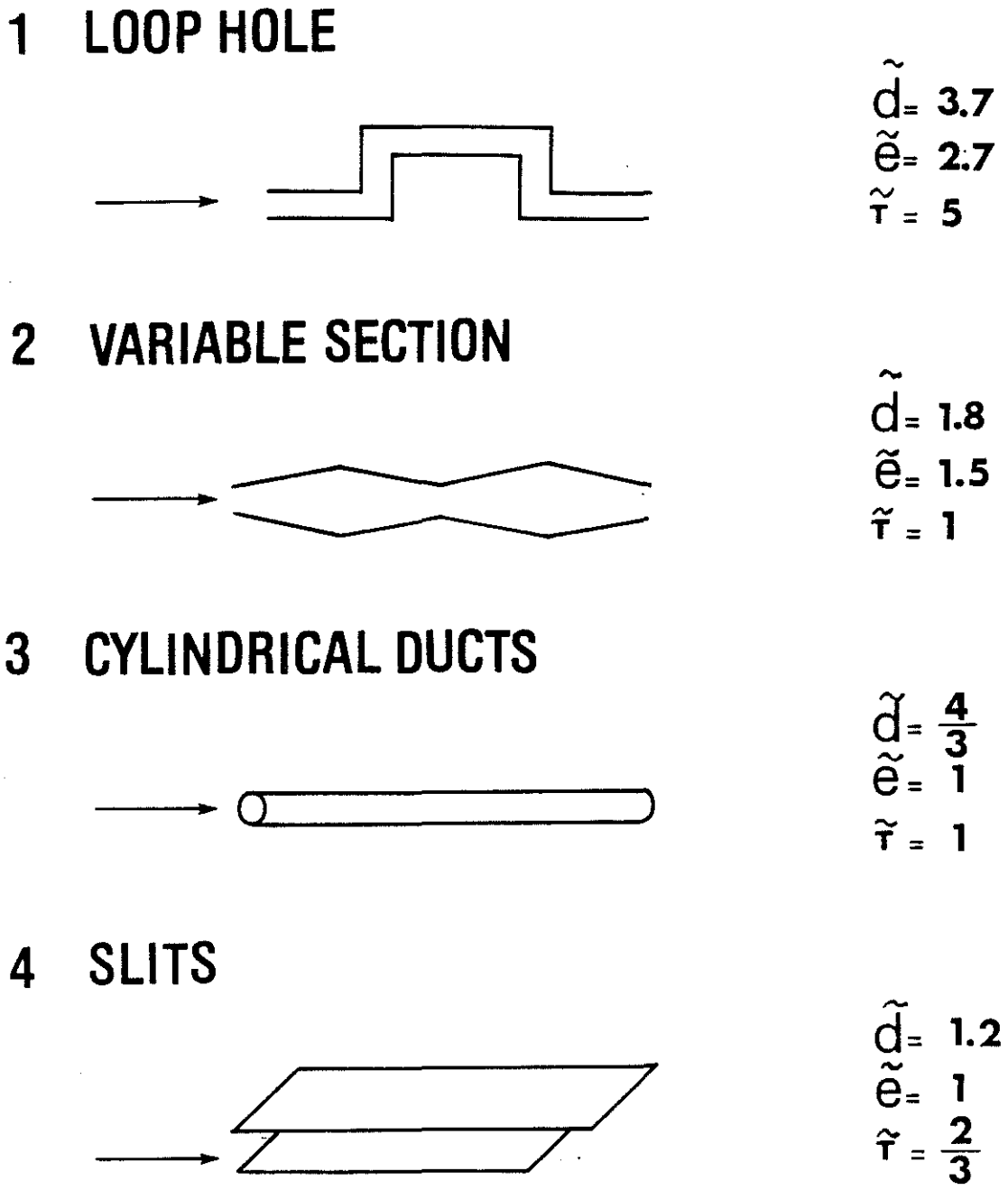

Figure 2: Pore models with a unidirectionl flow. $\tilde{d}$, and $\tilde{e}$ denote the low and high frequency limit of the mass coupling coefficient respectively. $\tilde{\tau}$ is the sinuosity.

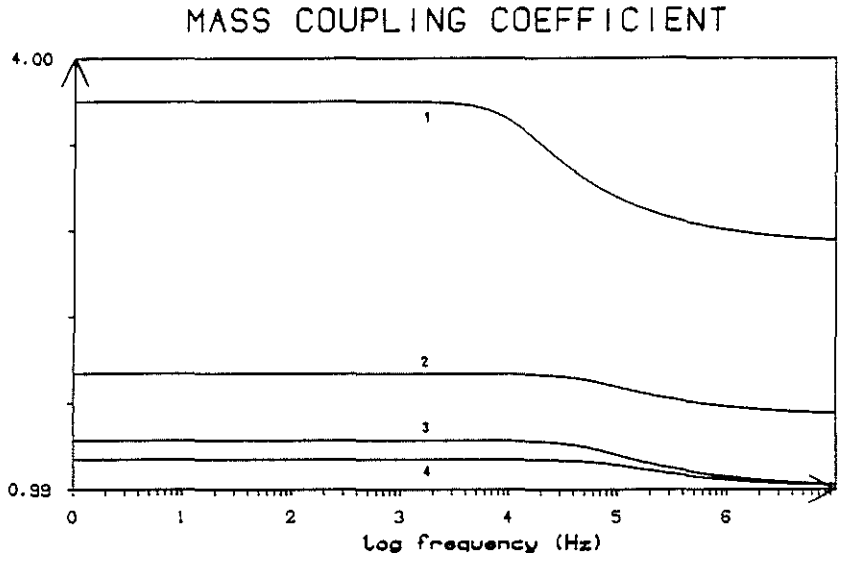

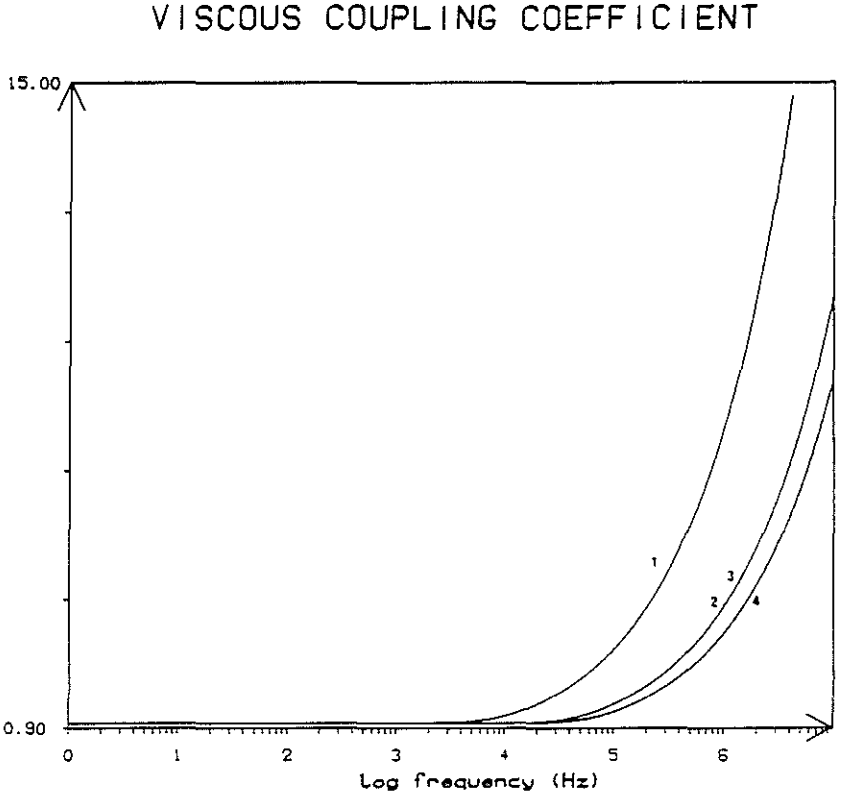

Figure 3a: Water saturated Teapot sandstone. $\tilde{\phi} = 29.7\%$, $\tilde{k} = 1.9$ darcy. Pore shape effects. The numbers refer to the models displayed on Figure 2. i.e.: 1: loop-hole, 2: (fictitious) variable section, 3: cylindrical duct, 4: plane slit.
Normalized coupling coefficients $(\rho_{22}(\omega)/(\tilde{\phi}\rho_f\ ; b(\omega)/(\eta\tilde{\phi}^2/\tilde{k}))$

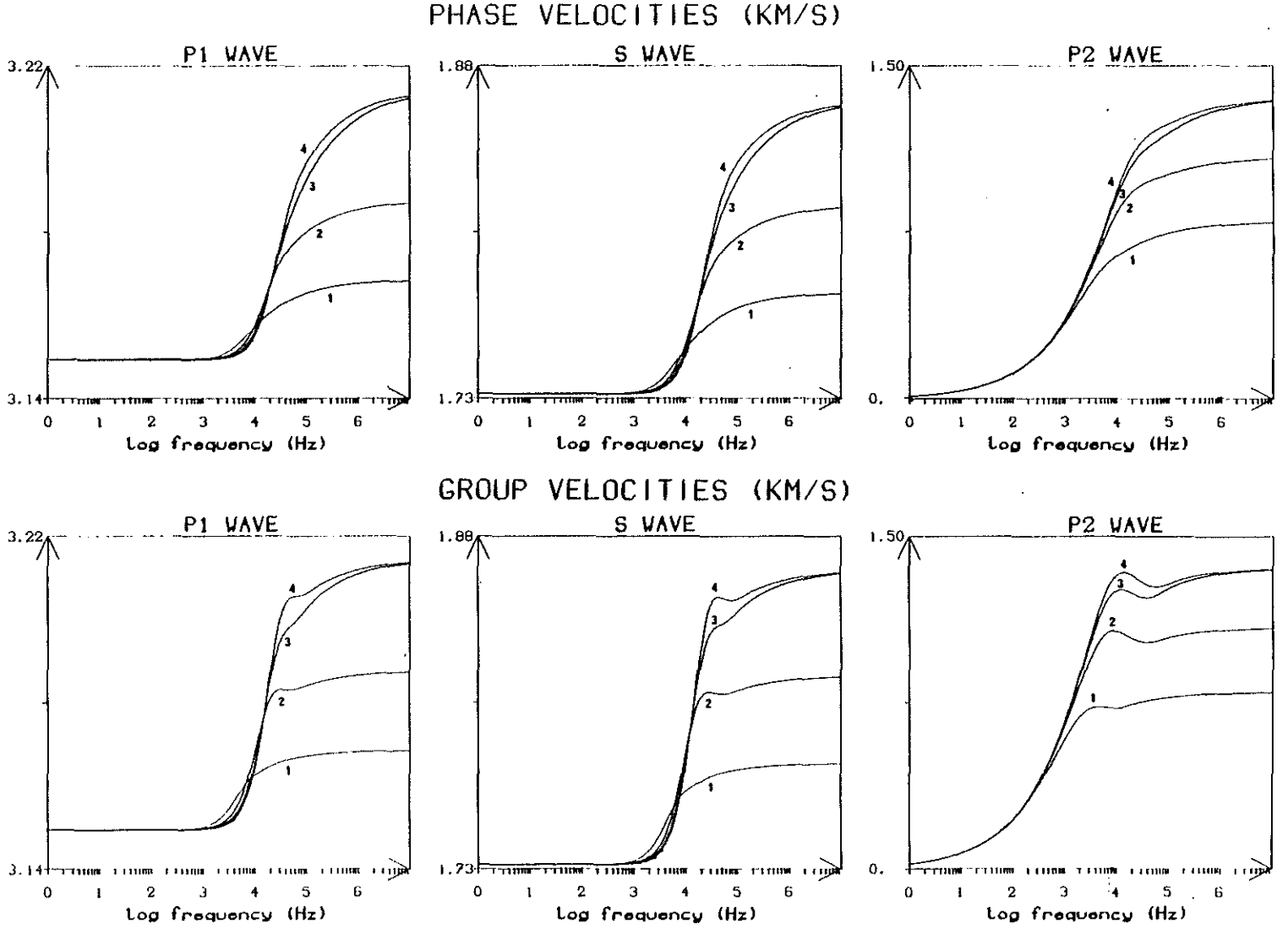

Figure 3b: Water saturated Teapot sandstone. $\tilde{\phi} = 29.7\%$, $\tilde{k} = 1.9$ darcy. Pore shape effects. The numbers refer to the models displayed on Figure 2. i.e.: 1: loop-hole, 2: (fictitious) variable section, 3: cylindrical duct, 4: plane slit.
Phase and group velocities of the body waves (P_1, S, P_2)

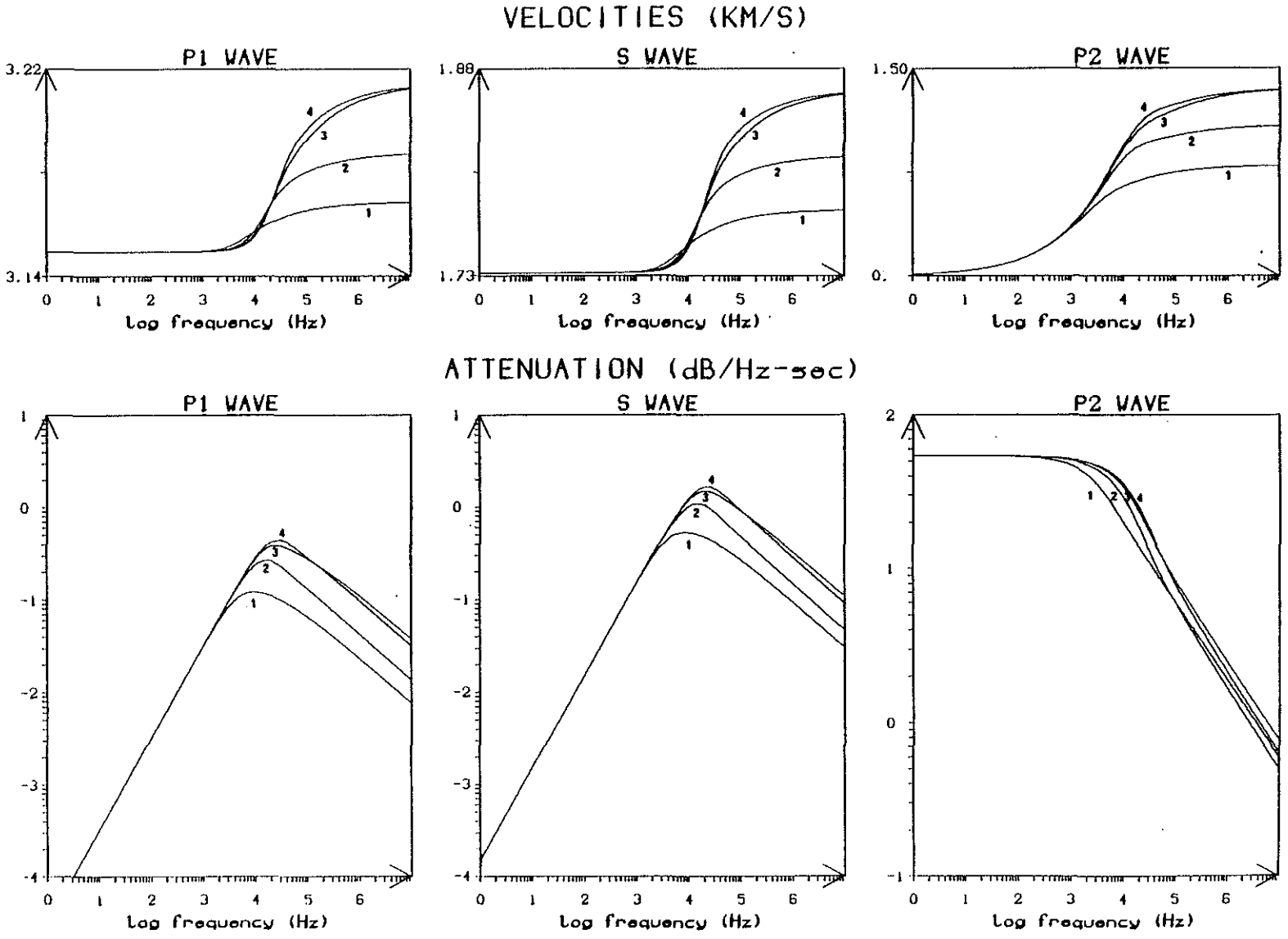

Figure 3c: Water saturated Teapot sandstone. $\tilde{\phi} = 29.7\%$, $\tilde{k} = 1.9$ darcy. Pore shape effects. The numbers refer to the models displayed on Figure 2. i.e.: 1: loop-hole, 2: (fictitious) variable section, 3: cylindrical duct, 4: plane slit.
Phase velocities and attenuations (dB/λ) of the body waves

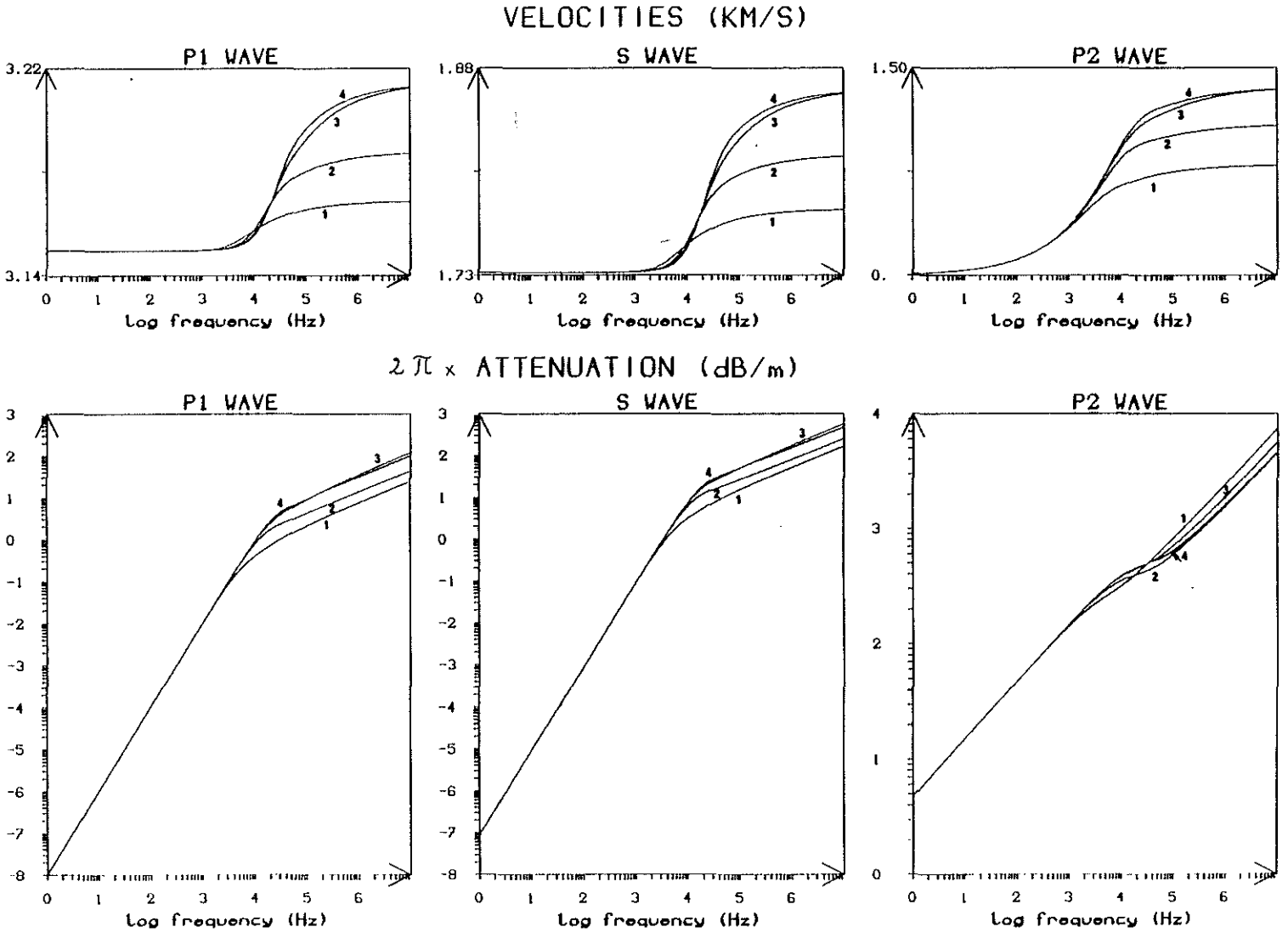

Figure 3d: Water saturated Teapot sandstone. $\tilde{\phi} = 29.7\%$, $\tilde{k} = 1.9$ darcy. Pore shape effects. The numbers refer to the models displayed on Figure 2. i.e.: 1: loop-hole, 2: (fictitious) variable section, 3: cylindrical duct, 4: plane slit.
Phase velocities and attenuations (dB/m) of the body waves

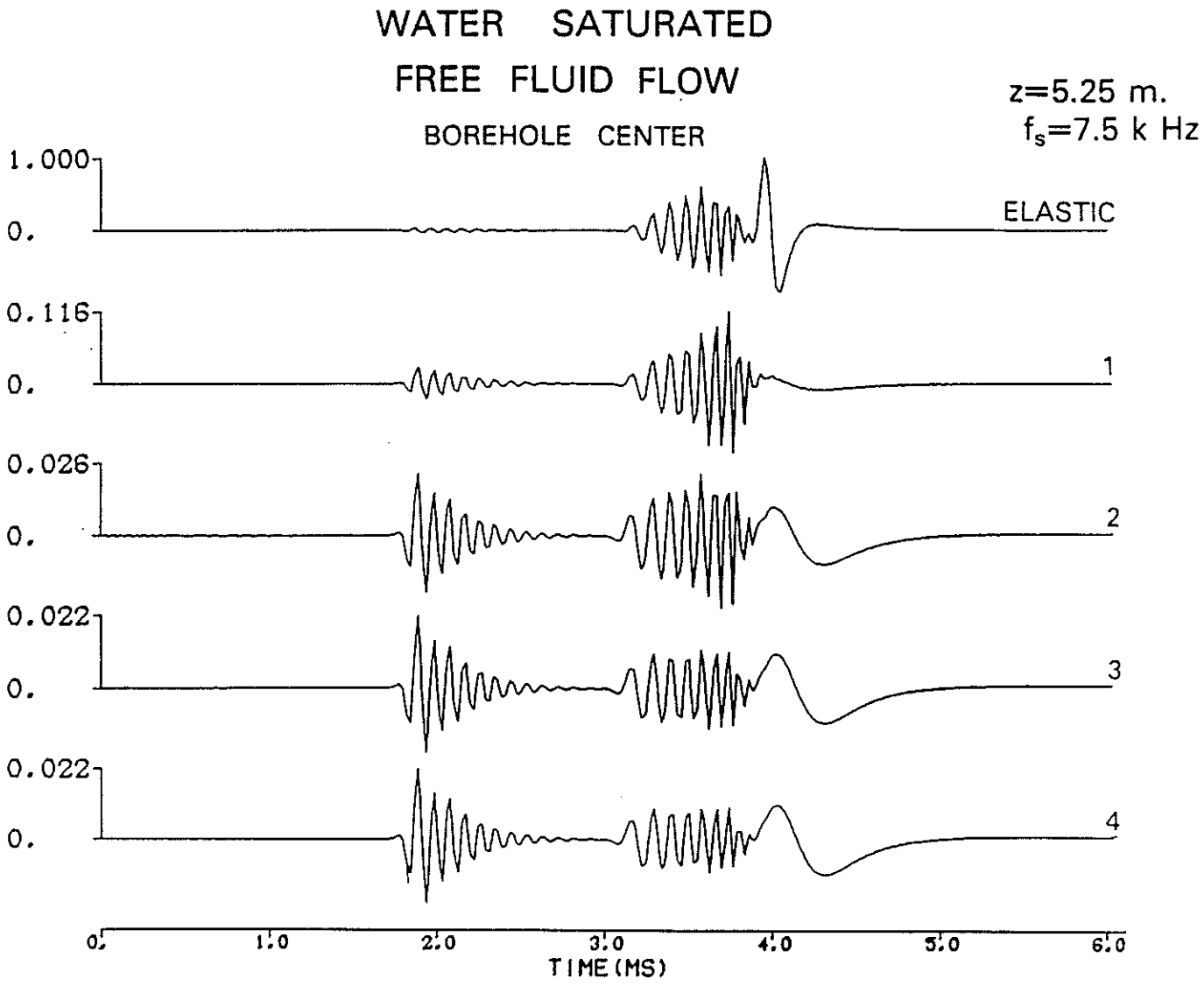

Figure 4: Water saturated Teapot sandstone. Permeable interface. Pore shape effects. Iso-offset (5.25 m) comparison of the synthetic microseismograms obtained at the center of a water filled borehole. The radius is equal to 10cm. The source center frequency is equal to 7.5 kHz. The numbers 1, 2, 3 and 4 refer to the models displayed on Figure 2. Each seismogram is normalized with respect to its own maximum.

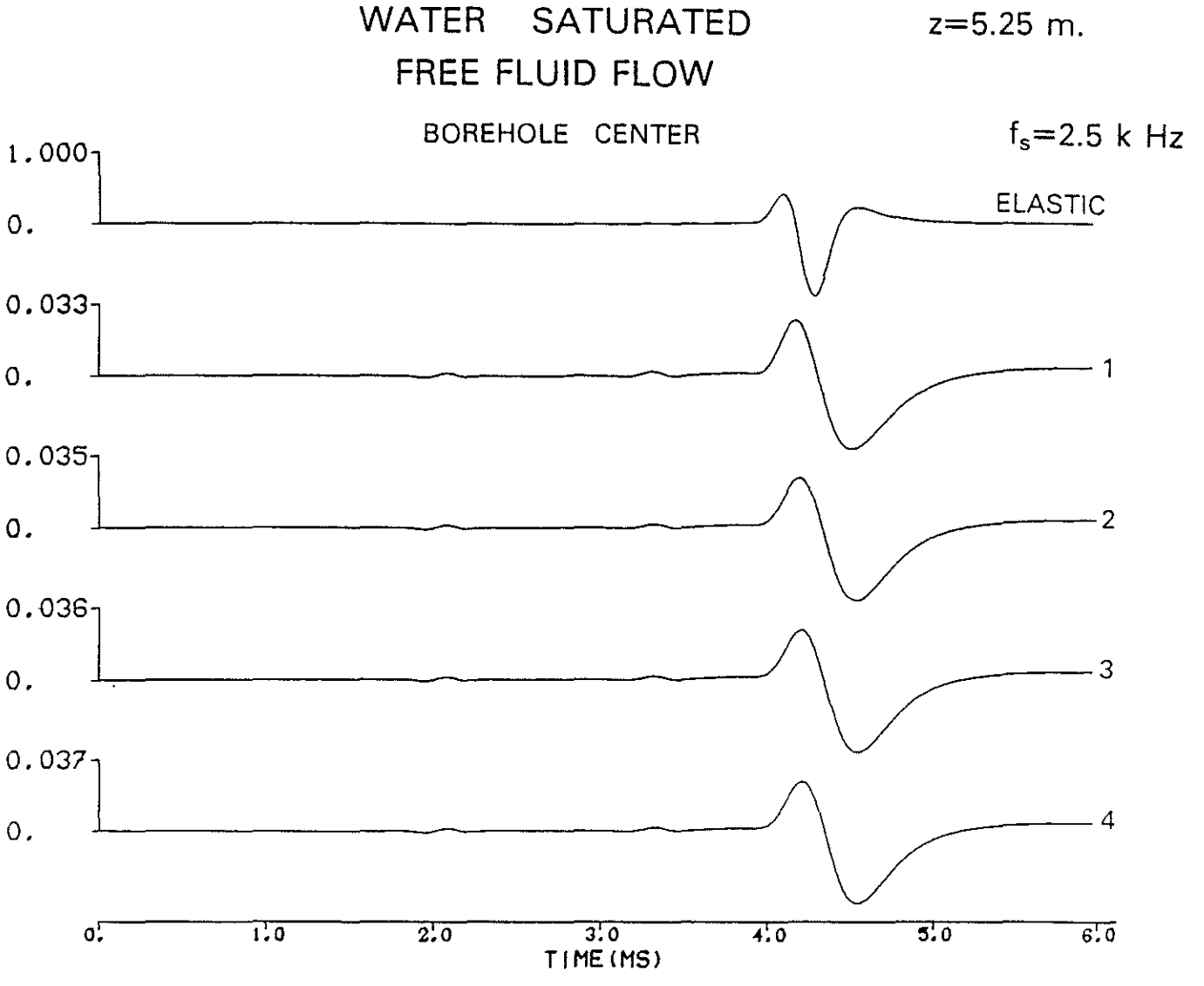

Figure 5: Same as Figure 4 with a 2.5 kHz source center frequency.

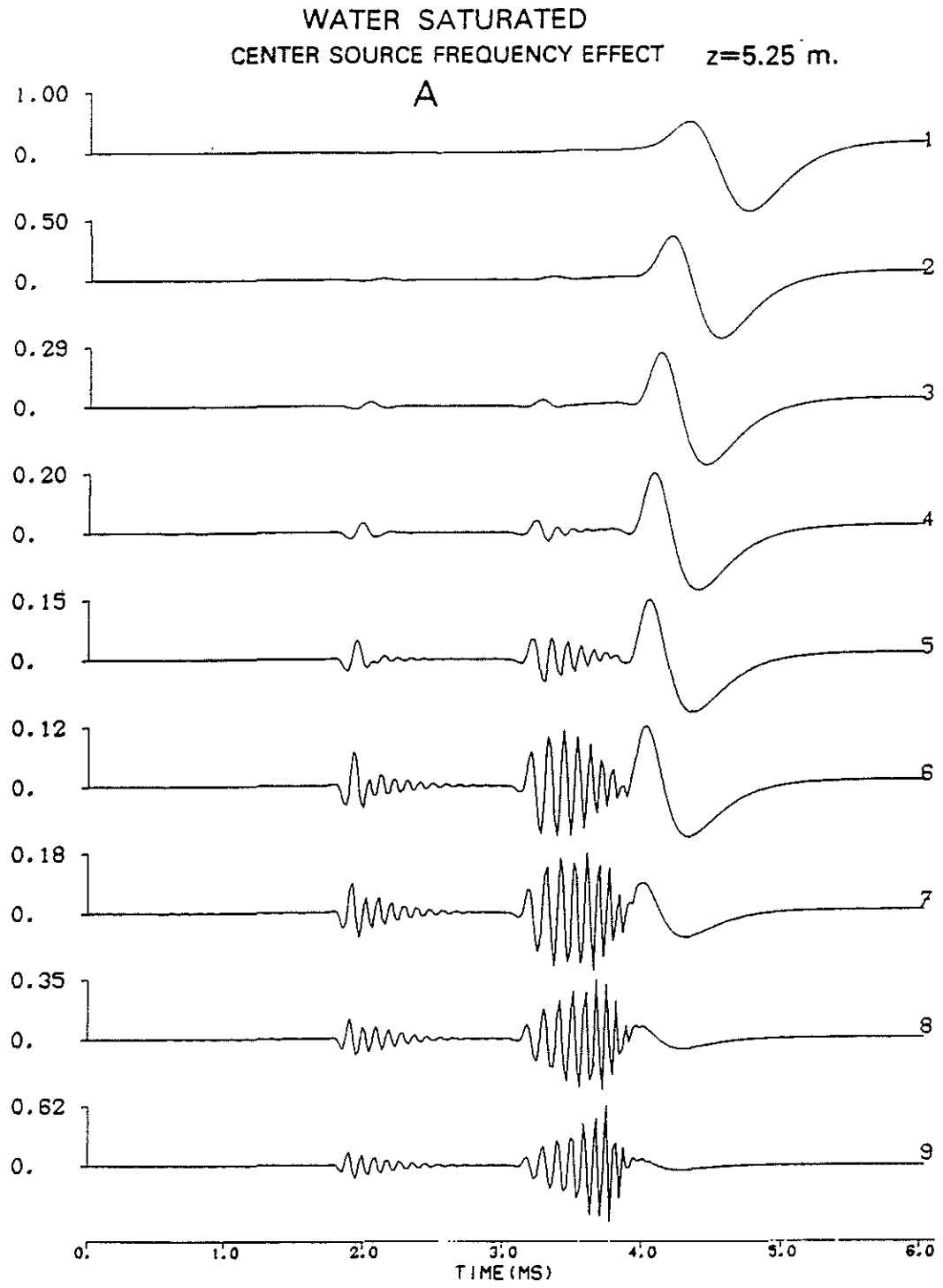

Figure 6A: Water saturated Teapot sandstone. Permeable interface. Pore shape and source center frequency effects. The offset is equal to 5.25 m and the calculations are performed at the borehole center (R = 10 cm). The pores are modelled as loop-holes (see Figure 2). The source center frequency varies from 1.5 kHz to 7.5 kHz by steps of 750 Hz from top to bottom. Each wavetrain is normalized with respect to its own maximum. Compare with Figure 6B.

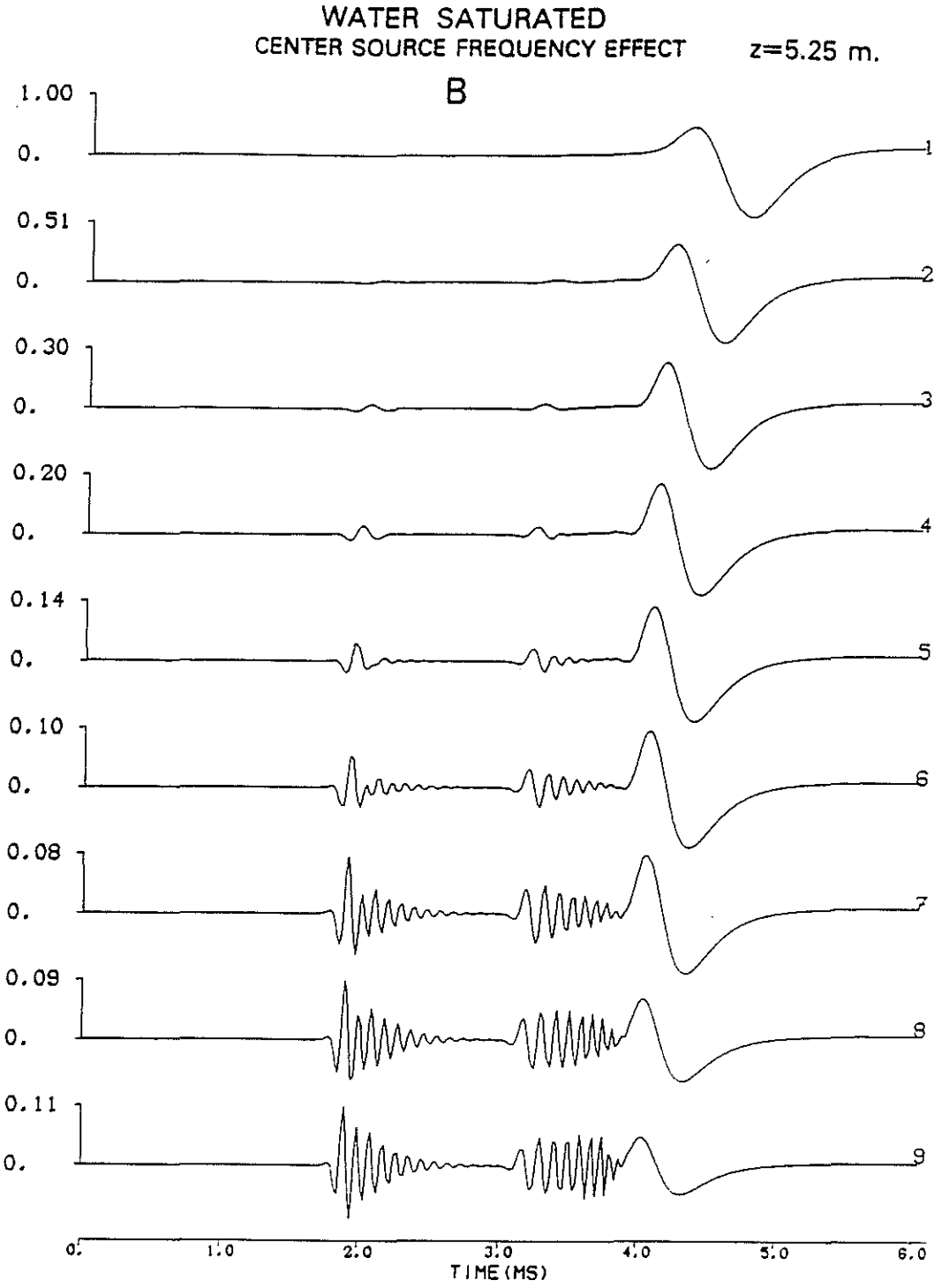

Figure 6B: Water saturated Teapot sandstone. Permeable interface. Pore shape and source center frequency effects. The offset is equal to 5.25 m and the calculations are performed at the borehole center (R = 10 cm). The pores are modelled as cylindrical ducts (see Figure 2). The source center frequency varies from 1.5 kHz to 7.5 Khz by steps of 750 Hz from top to bottom. Each wavetrain is normalized with respect to its own maximum. Compare with Figure 6A.

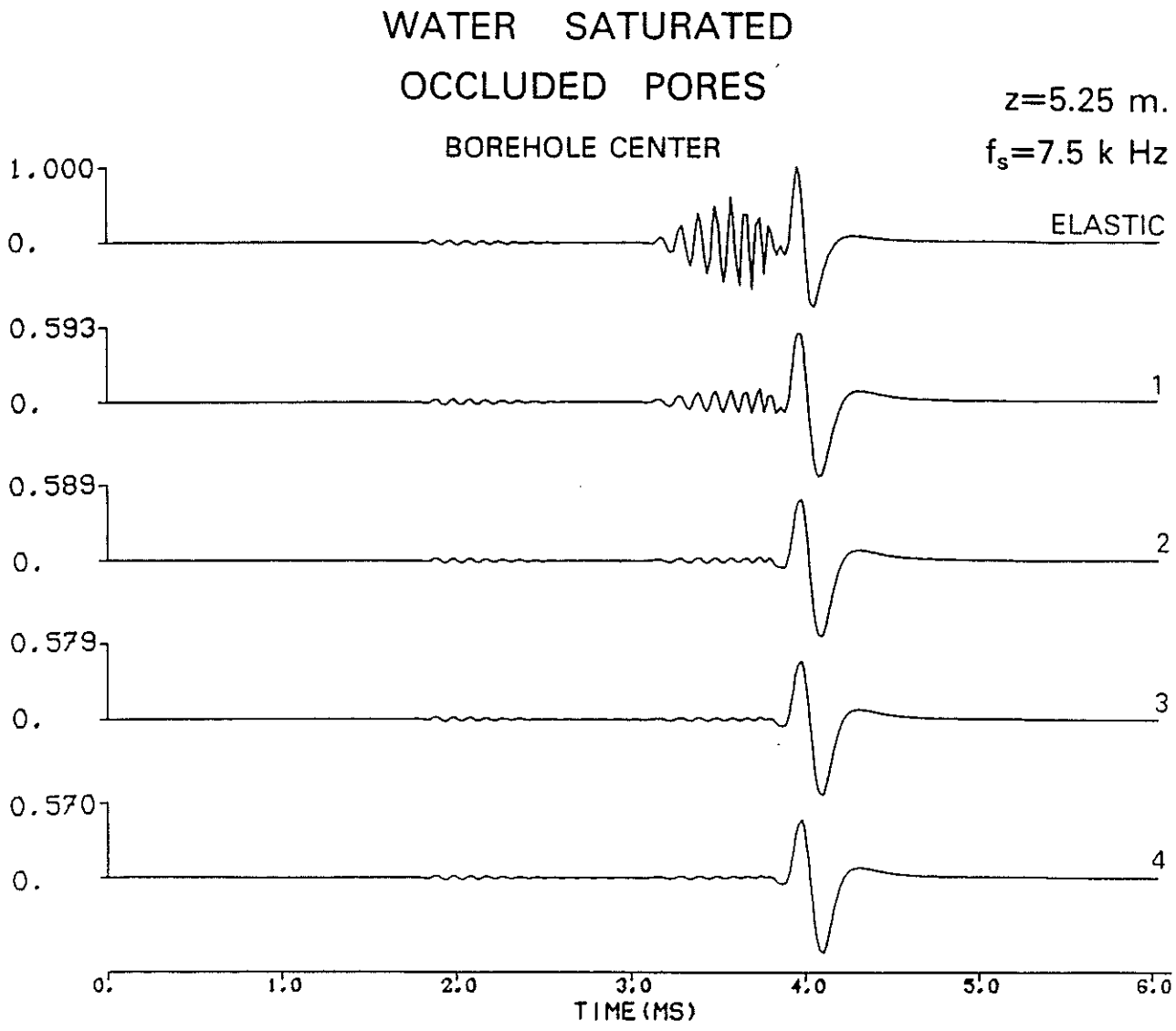

Figure 7: Water saturated Teapot sandstone ($\tilde{\phi} = 29.7\%$, $\tilde{k} = 1.9$ darcy). Impermeable interface. Pore shape effects. Iso-offset (5.25 m) comparison of the synthetic microseismograms at the center of a water filled borehole (R = 10cm). 1, 2, 3, 4 refer to the pore models displayed on Figure 2. Each waveform is normalized with respect to its own maximum. The source center frequency is equal to 7.5 kHz.

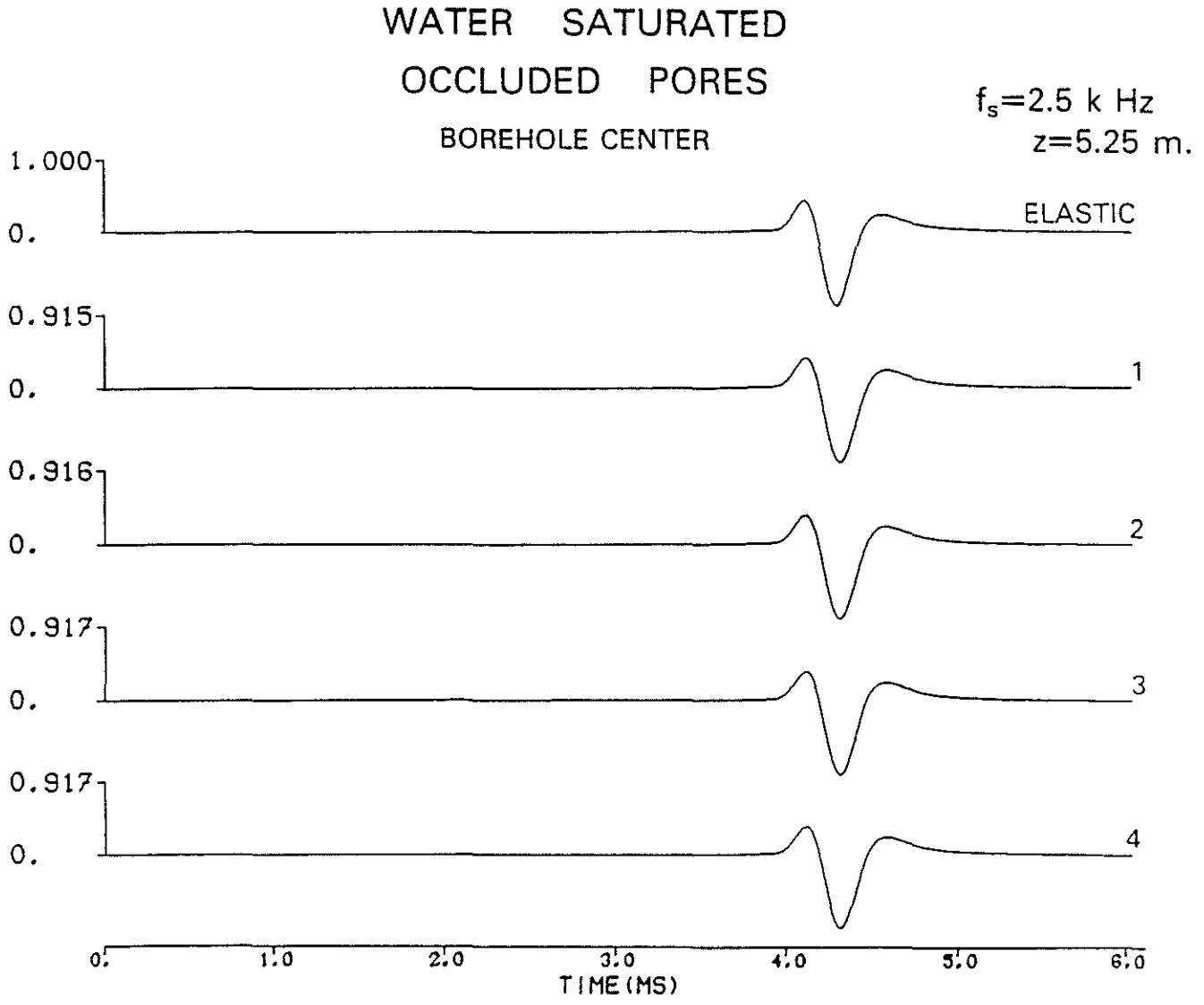

Figure 8: Same as Figure 7 with a 2.5 kHz source center frequency.

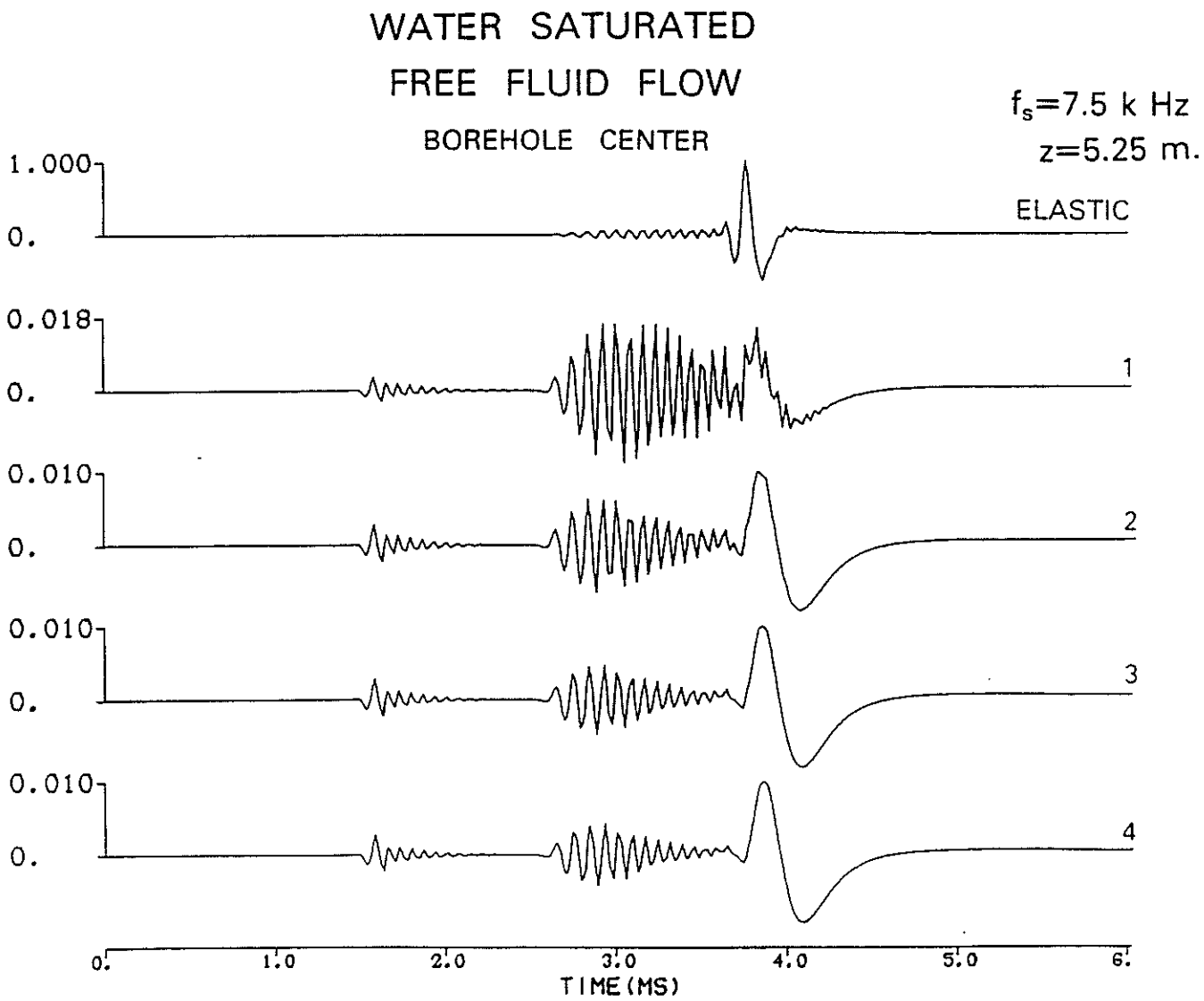

Figure 9: Water saturated Berea sandstone ($\tilde{\phi} = 19\%$, $\tilde{k} = 1$ darcy). Permeable interface. Pore shape effects. Iso-offset (5.25 m) comparison of the synthetic microseismograms obtained at the center of a water filled borehole (R = 7cm). The numbers 1, 2, 3 and 4 refer to the pore model displayed on Figure 2. The source center frequency is equal to 7.5 kHz. Each waveform is normalized with respect to its own maximum.

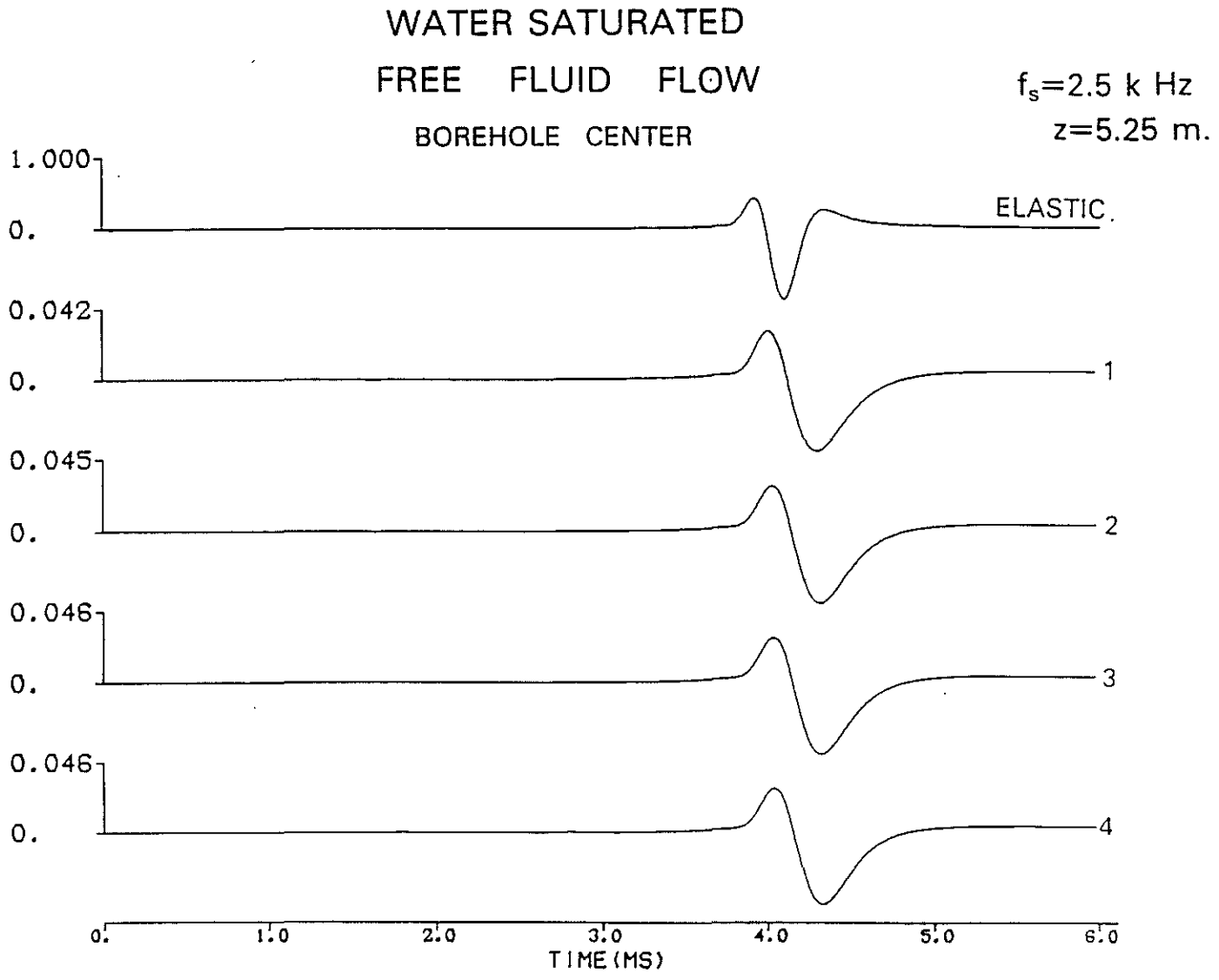

Figure 10: Same as Figure 9 with a 2.5 kHz source center frequency.

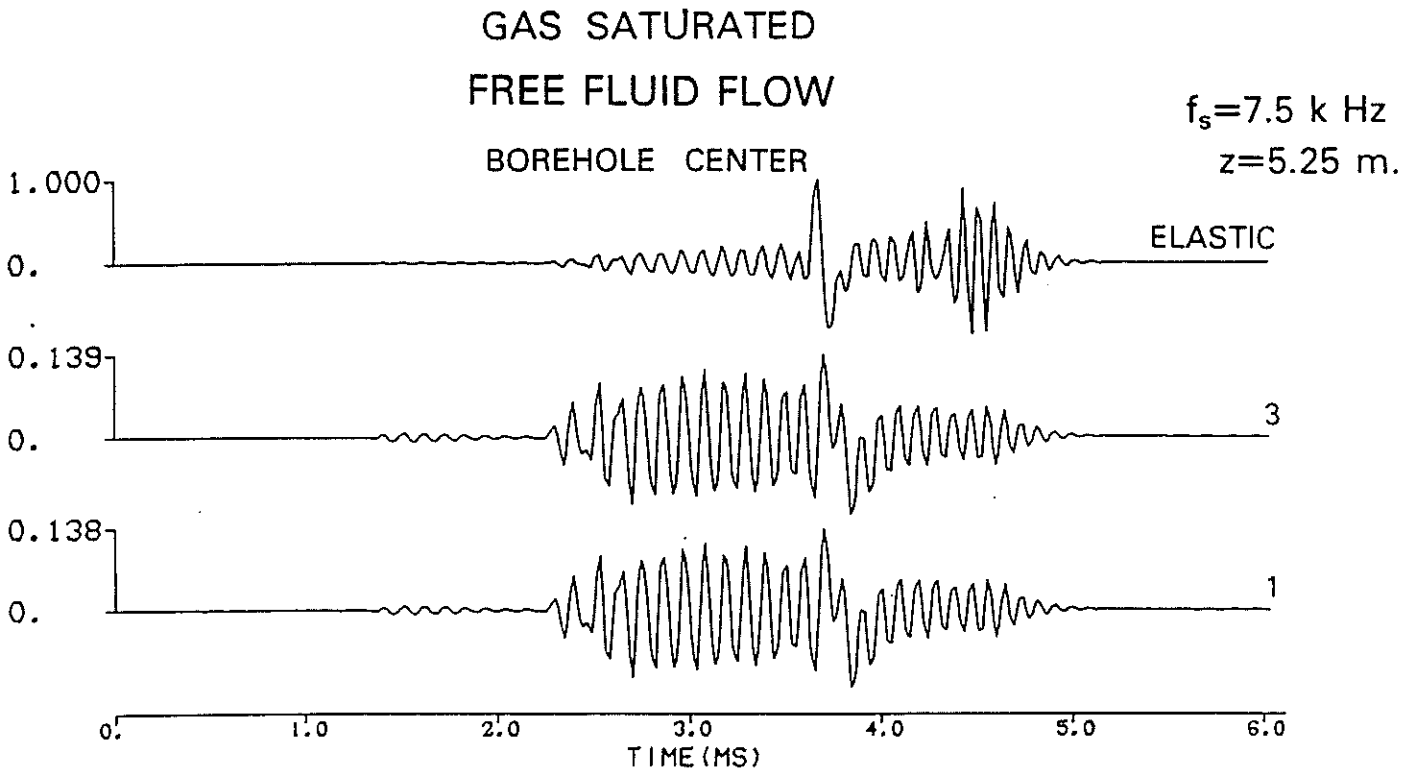

Figure 11: Gas saturated Fox Hill sandstone ($\tilde{\phi} = 7.4\%$, $\tilde{k} = 1$ millidarcy). Permeable interface. Pore shape effects. Iso-offset (5.25 m) comparison of the synthetic microseismograms obtained at the center of a water filled borehole (R = 10 cm). The numbers 1 and 3 refer to the pore models displayed on Figure 2. The source center frequency is equal to 7.5 kHz. Each waveform is normalized with respect to its own maximum.

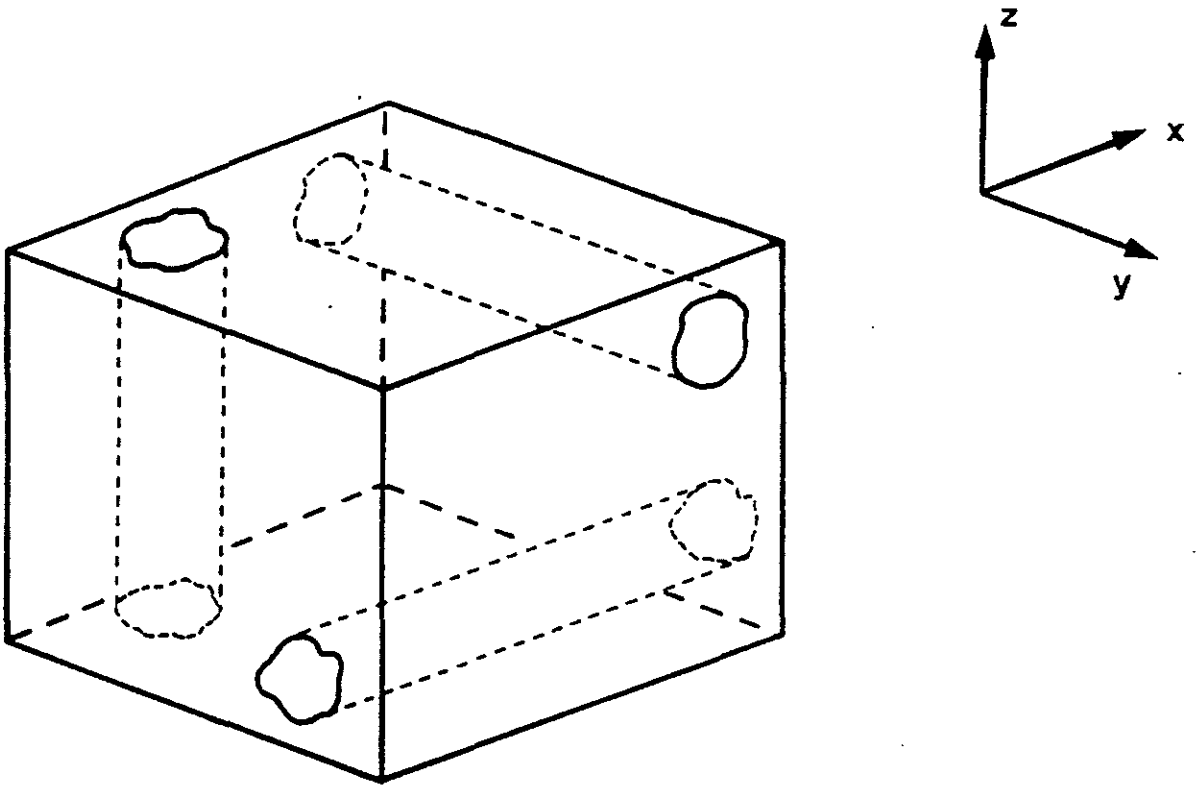

Figure 12: Distribution of non interconnected cylindrical ducts along perpendicular directions.

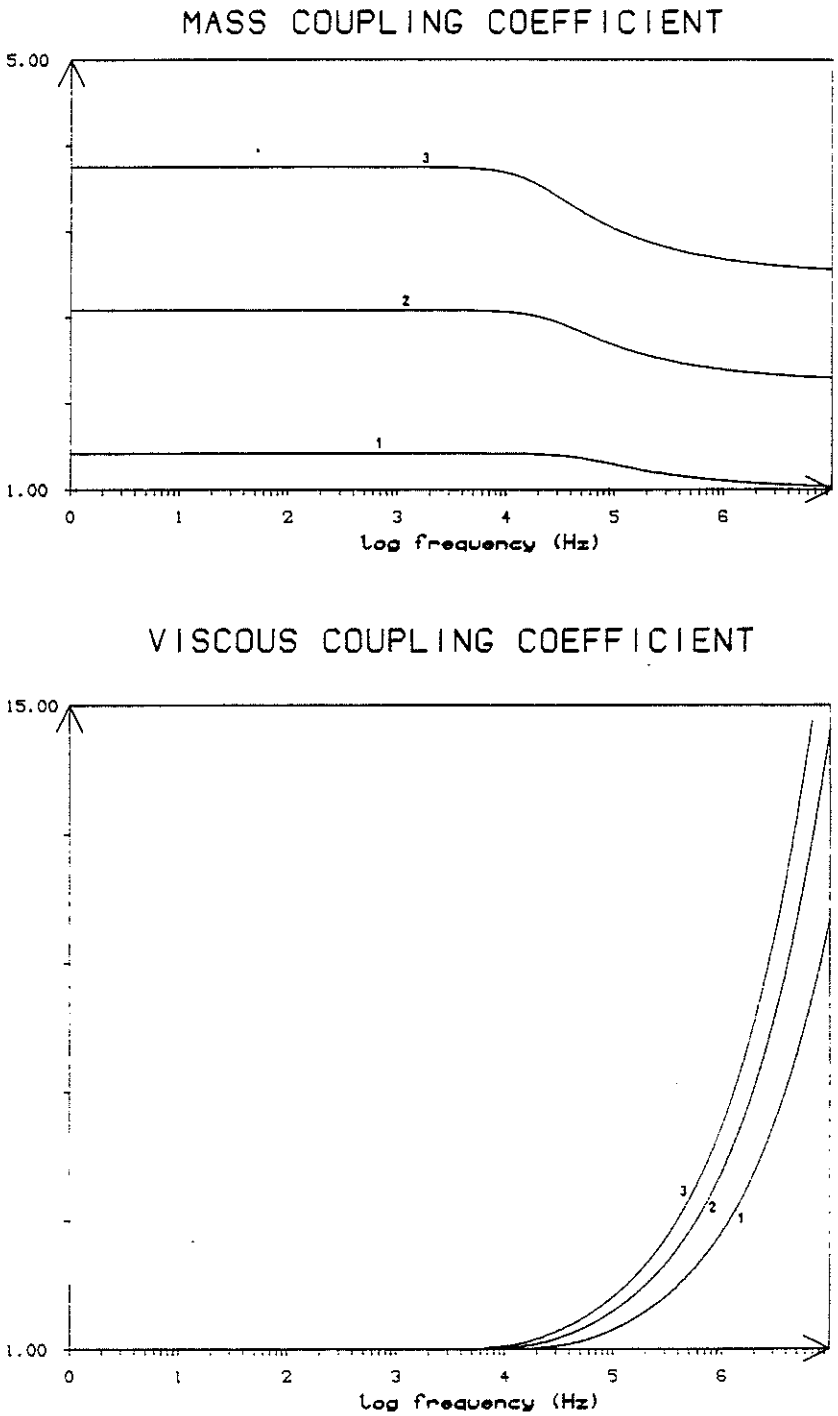

Figure 13a: Water saturated Teapot sandstone ($\tilde{\phi} = 29.7\%$, $\tilde{k} = 1.9$ darcy). Effects of the distribution along perpendicular directions of non interconnected cylindrical ducts. The numbers 1, 2 and 3 refer to the number of perpendicular directions taken into account. Normalized coupling coefficients $(\rho_{22}(\omega)/(\tilde{\phi}\rho_f\,; b(\omega)/(\eta\tilde{\phi}^2/\tilde{k}))$

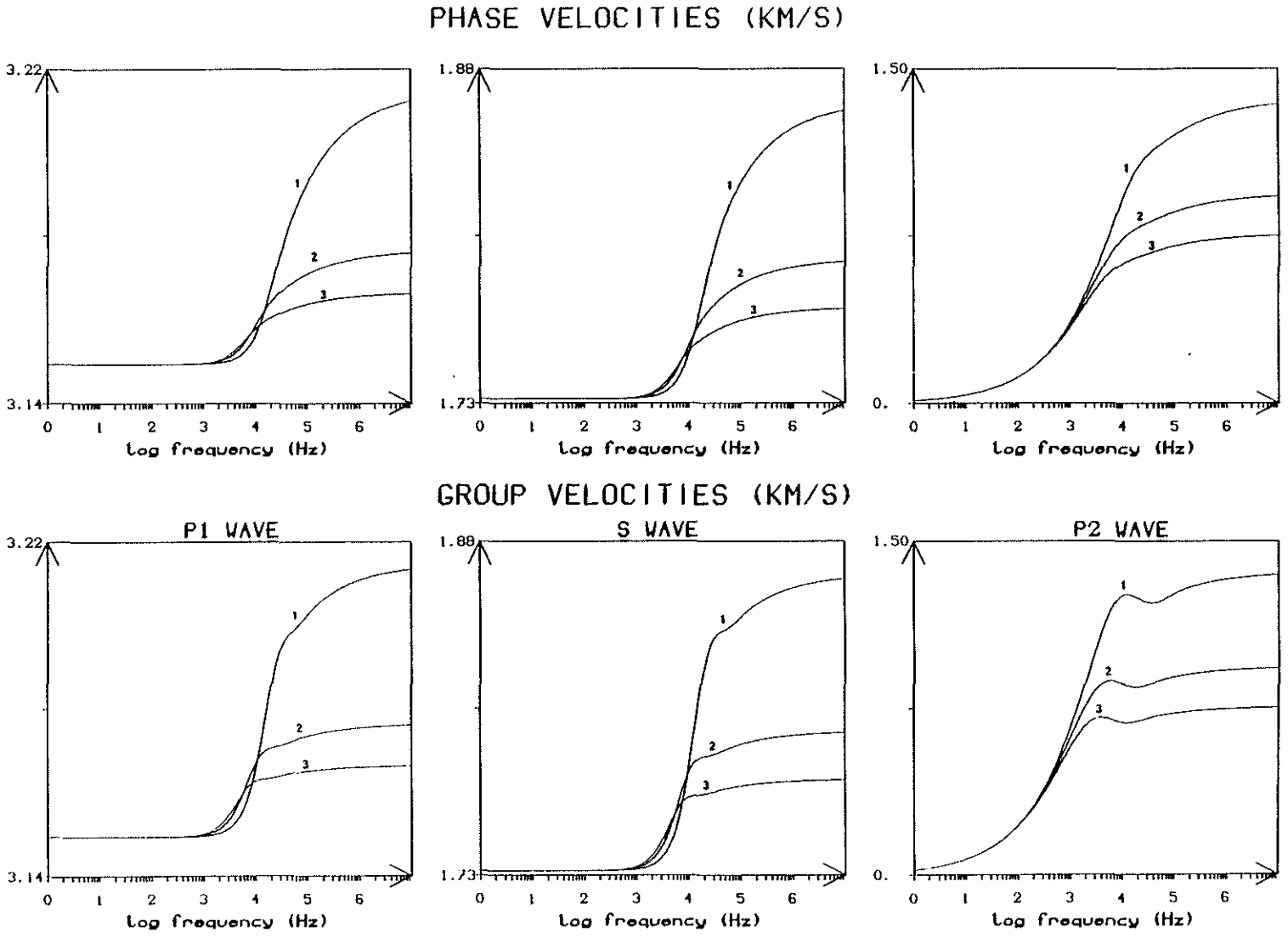

Figure 13b: Water saturated Teapot sandstone ($\tilde{\phi} = 29.7\%$, $\tilde{k} = 1.9$ darcy). Effects of the distribution along perpendicular directions of non interconnected cylindrical ducts. The numbers 1, 2 and 3 refer to the number of perpendicular directions taken into account. Phase and group velocities of the body waves (P_1, S, P_2)

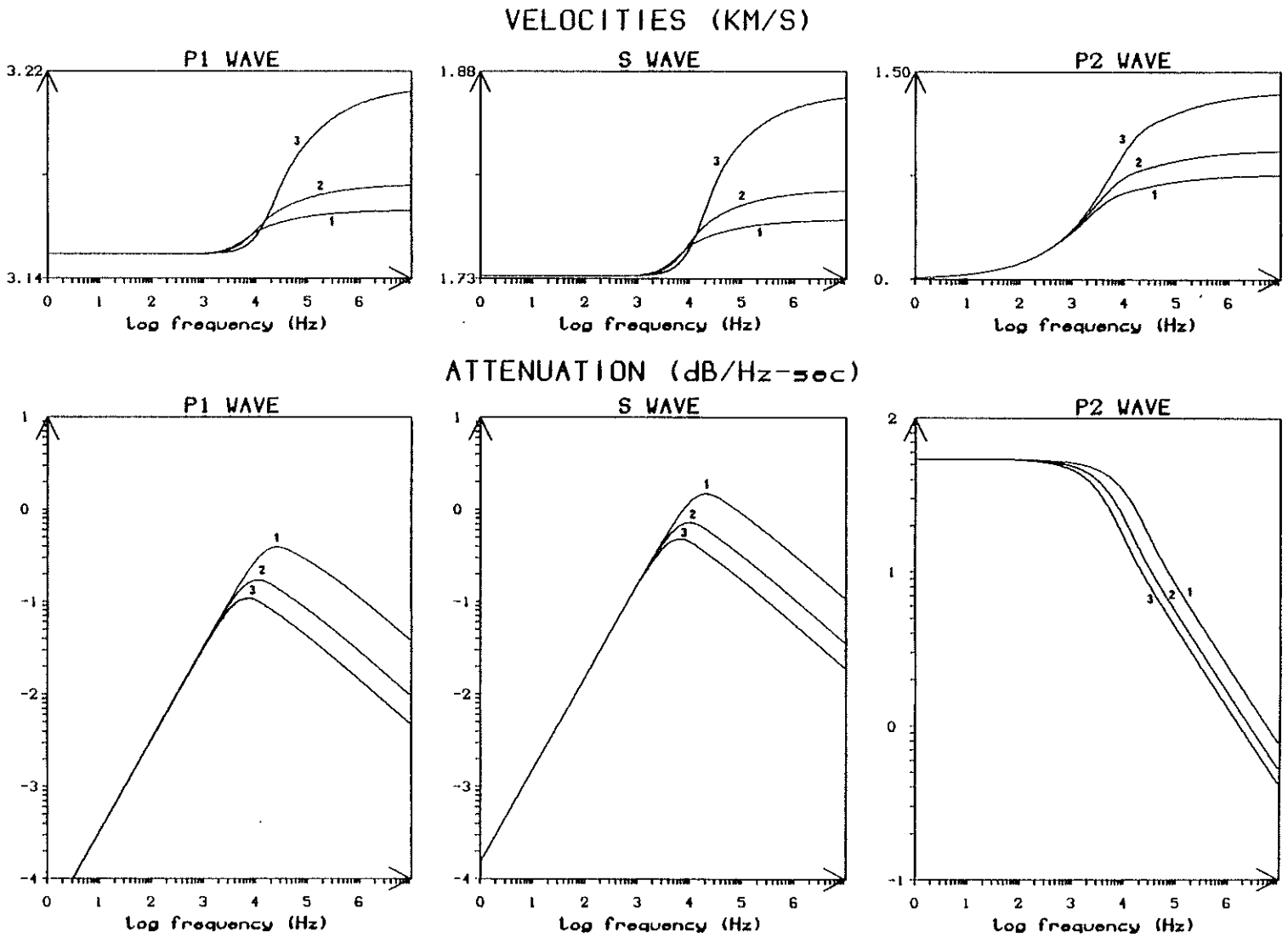

Figure 13c: Water saturated Teapot sandstone ($\tilde{\phi} = 29.7\%$, $\tilde{k} = 1.9$ darcy). Effects of the distribution along perpendicular directions of non interconnected cylindrical ducts. The numbers 1, 2 and 3 refer to the number of perpendicular directions taken into account. Phase velocities and attenuations (dB/λ) of the body waves

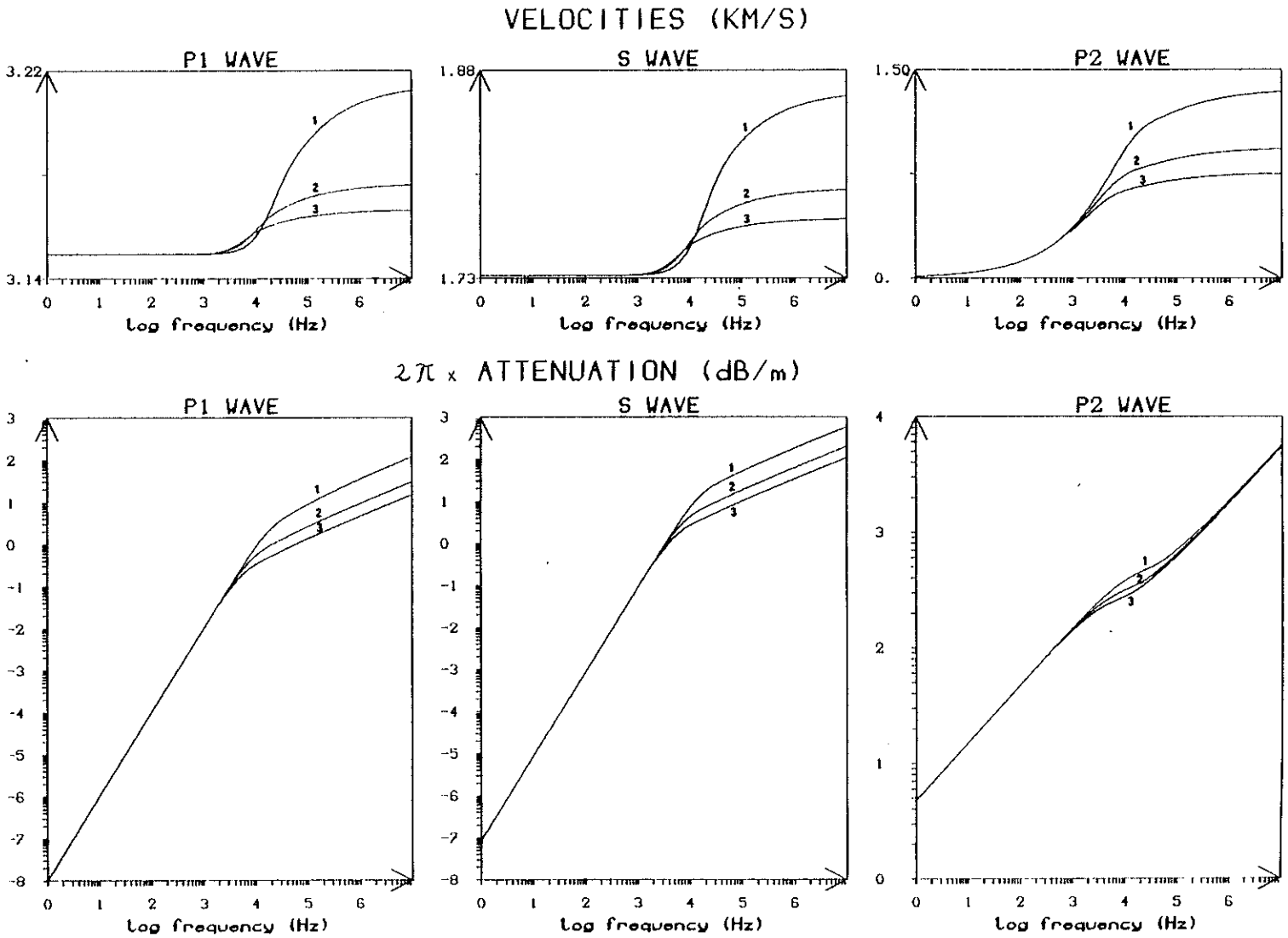

Figure 13d: Water saturated Teapot sandstone ($\tilde{\phi} = 29.7\%$, $\tilde{k} = 1.9$ darcy). Effects of the distribution along perpendicular directions of non interconnected cylindrical ducts. The numbers 1, 2 and 3 refer to the number of perpendicular directions taken into account. Phase velocities and attenuations (dB/m) of the body waves

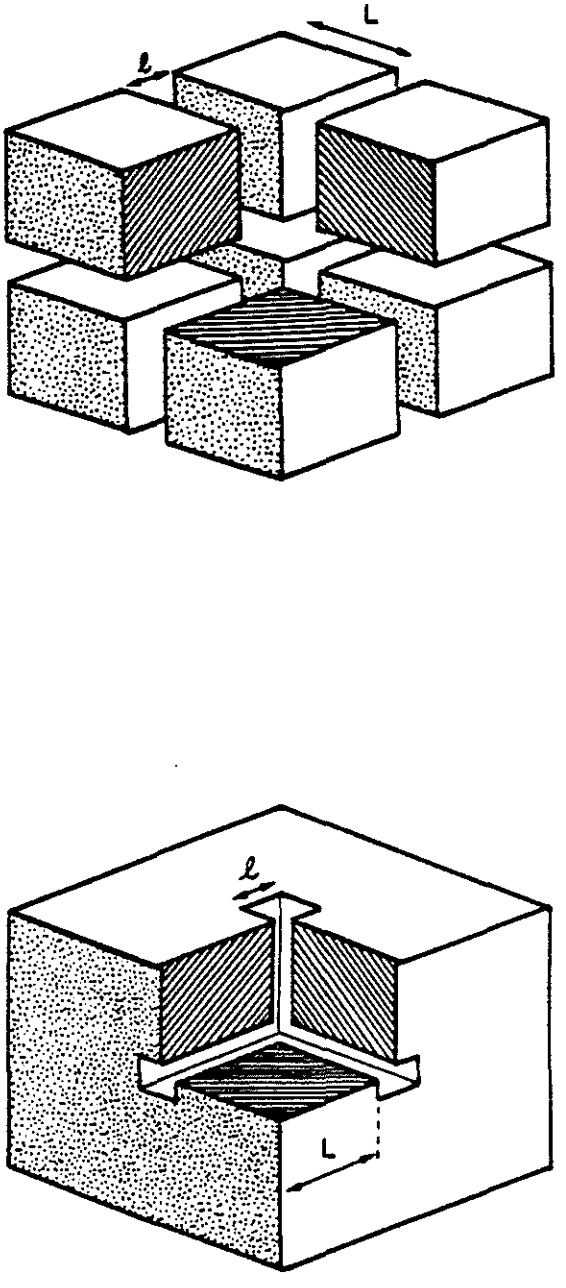

Figure 14a, b: Examples of orthotropic materials which include interconnected pores.